JGR Planets

RESEARCH ARTICLE

10.1029/2024JE008576

Magma Ocean Evolution at Arbitrary Redox State

Harrison Nicholls[1], Tim Lichtenberg[2], Dan J. Bower[3,4], and Raymond Pierrehumbert[1]

[1]Atmospheric, Oceanic and Planetary Physics, University of Oxford, Oxford, UK, [2]Kapteyn Astronomical Institute, University of Groningen, Groningen, The Netherlands, [3]Center for Space and Habitability, University of Bern, Bern, Switzerland, [4]Institute of Geochemistry and Petrology, ETH Zurich, Zürich, Switzerland

Key Points:

- Atmospheres overlying magma oceans can have diverse volatile compositions depending on mantle redox and volatile endowment
- Magma oceans on Earth-like planets may not solidify, retaining substantial melt fractions, and hence volatiles, in their interiors
- While initially convective, modeling indicates that these atmospheres may become convectively stable in the later stages of their evolution

Correspondence to:

H. Nicholls,
harrison.nicholls@physics.ox.ac.uk

Citation:

Nicholls, H., Lichtenberg, T., Bower, D. J., & Pierrehumbert, R. (2024). Magma ocean evolution at arbitrary redox state. *Journal of Geophysical Research: Planets*, *129*, e2024JE008576. https://doi.org/10.1029/2024JE008576

Received 3 JUL 2024
Accepted 28 NOV 2024

Author Contributions:

Conceptualization: Harrison Nicholls, Tim Lichtenberg, Raymond Pierrehumbert
Data curation: Harrison Nicholls
Formal analysis: Harrison Nicholls
Investigation: Harrison Nicholls
Methodology: Harrison Nicholls, Raymond Pierrehumbert
Resources: Raymond Pierrehumbert
Software: Harrison Nicholls, Dan J. Bower
Supervision: Raymond Pierrehumbert
Validation: Harrison Nicholls
Visualization: Harrison Nicholls
Writing – original draft: Harrison Nicholls
Writing – review & editing: Harrison Nicholls, Tim Lichtenberg, Dan J. Bower, Raymond Pierrehumbert

Abstract Interactions between magma oceans and overlying atmospheres on young rocky planets leads to an evolving feedback of outgassing, greenhouse forcing, and mantle melt fraction. Previous studies have predominantly focused on the solidification of oxidized Earth-similar planets, but the diversity in mean density and irradiation observed in the low-mass exoplanet census motivate exploration of strongly varying geochemical scenarios. We aim to explore how variable redox properties alter the duration of magma ocean solidification, the equilibrium thermodynamic state, melt fraction of the mantle, and atmospheric composition. We develop a 1D coupled interior-atmosphere model that can simulate the time-evolution of lava planets. This is applied across a grid of fixed redox states, orbital separations, hydrogen endowments, and C/H ratios around a Sun-like star. The composition of these atmospheres is highly variable before and during solidification. The evolutionary path of an Earth-like planet at 1 AU ranges between permanent magma ocean states and solidification within 1 Myr. Recently solidified planets typically host H_2O- or H_2-dominated atmospheres in the absence of escape. Orbital separation is the primary factor determining magma ocean evolution, followed by the total hydrogen endowment, mantle oxygen fugacity, and finally the planet's C/H ratio. Collisional absorption by H_2 induces a greenhouse effect which can prevent or stall magma ocean solidification. Through this effect, as well as the outgassing of other volatiles, geochemical properties exert significant control over the fate of magma oceans on rocky planets.

Plain Language Summary The mantle of modern Earth is solid. However, young planets could have (partially) molten mantles which enable rapid transport of gases and energy to the surface. Such mantles are termed "magma oceans." We explore how the properties of a planet determine magma ocean duration and study what kinds of atmospheres are produced by outgassing. We do this by developing a computational model to simulate their evolution over time, which is then applied to an Earth-like planet over a range of different conditions. Our simulations show that the composition of atmospheres on magma ocean planets is highly variable. However, recently solidified planets typically host hot atmospheres containing large amounts of water vapor. Evolutionary timescales also cover a wide range, with some planets maintaining permanent magma oceans while others rapidly solidify. While the main factor determining magma ocean evolution is orbital separation, insulation by the greenhouse effects of H_2 and H_2O can act to prevent or slow down their solidification. It is important to consider the geochemical properties of planetary magma oceans, as these influence the composition of overlying atmospheres.

1. Introduction

It is thought that the Earth, the Moon, Mars, and Venus have all been partially or entirely molten at least once in their lifetimes, maintaining a so-called "magma ocean" (Elkins-Tanton, 2008; Nakajima et al., 2021; Tonks & Melosh, 1993; Warren, 1985). Direct measurements of KREEP elements in lunar samples provide strong evidence for this (Borg et al., 2004; Korotev & Gillis, 2001; Warren & Wasson, 1979). These bodies now maintain solid interiors and exhibit various conditions above their surfaces in terms of atmospheric pressure, composition, temperature, and radiation. An exception to this that recent measurements indicate the presence of a liquid silicate layer deep within the interior of Mars (Khan et al., 2023). The evolutionary divergence between Venus and Earth has been suggested to result from the feedback between irradiation, melting, greenhouse forcing and atmospheric escape (Hamano et al., 2013; Turbet et al., 2021). The vast majority of observed exoplanets orbit within the classical runaway greenhouse instellation threshold, where planets may enter a permanent magma ocean state until their atmospheric volatile inventory is depleted by escape processes (Ikoma et al., 2018; Massol et al., 2016). It has been argued that a more realistic post-runaway steady state may not be compatible with a permanent magma ocean. Selsis et al. (2023) used radiative-convective models to simulate pure-steam atmospheres under various instellations, finding that the formation of deep isothermal layers allows global radiative equilibrium to be

achieved with relatively cool surface temperatures. This indicates that a larger instellation than previously thought may be required to sustain a permanent magma ocean. However, they did not simulate the time-evolution of magma oceans from an initially molten state. Nor did they account for a broad range of opacity sources, such as from gases other than water vapor.

Understanding the nature of magma ocean evolution is thus of primary importance for resolving the link between a planet's initial conditions and its current state, as it is contemporaneous with stellar evolution and atmospheric escape, as well as providing the initial conditions for potential future geochemical cycling of volatiles through a solidified mantle (Lichtenberg et al., 2023). Magma oceans of various depths may occur on planets between giant impact events, influencing the distribution of volatiles and their susceptibility to impact erosion (Gu et al., 2024). Whether generated by stochastic giant impacts or originating from more continuous accretion processes during planet formation, these molten planets are initially self-luminous, rapidly cooling until they reach global radiative equilibrium (Bonati et al., 2019; Salvador et al., 2023; Krissansen-Totton, 2023). Global radiative equilibrium may be sustained by a range of possible conditions; a planet may reach radiative equilibrium before or after complete crystallization, which determines whether or not the planet can maintain a permanent magma ocean (Chao et al., 2021; Lichtenberg & Miguel, 2024). The thermal stratification of runaway greenhouse climates has been suggested as an observational signature to probe via exoplanet surveys (Schlecker et al., 2024; Turbet et al., 2019).

Some volatile species (such as H_2O) are highly soluble in molten rock, allowing significant volatile inventories to be stored within molten interiors (Hamilton et al., 1964; Sossi et al., 2020, 2023; Suer et al., 2023). For planets orbiting young stars this could buffer such atmospheres against escape, thereby allowing them to maintain atmospheres for longer, and/or could trap volatiles inside the interior once the planet has solidified (Bower et al., 2022; Dorn & Lichtenberg, 2021; Hamano et al., 2015). The cooling timescale and crystallization mode of a magma ocean may depend on the thermal blanketing of a radiatively absorbing atmosphere, since outgassing of sufficiently opaque gases (e.g., H_2O, CO_2, and H_2) could induce a strong enough greenhouse effect to significantly delay cooling of the planet (Bower et al., 2022; Lichtenberg et al., 2021; Nikolaou et al., 2019; R. T. Pierrehumbert, 2010; Salvador et al., 2017; Spada et al., 2013). The composition of the atmosphere overlying a magma ocean is thought to be strongly tied to the properties of the mantle due to the rapid volatile exchange between the two inventories (Lichtenberg, 2021; Spaargaren et al., 2020). Given that planetary interiors are expected to span a range of geochemical conditions (Krijt et al., 2023), it is prudent to explore how magma ocean evolution depends on these properties (Guimond et al., 2023; Krissansen-Totton et al., 2021).

In this work, we focus on the impact of interior properties and initial volatile endowment on the evolution of planetary magma oceans in the absence of external loss and delivery processes (e.g., escape). This is done with the aim of understanding how outgassing and energy transport alone shape planetary evolution and solidification outcomes.

2. Methods

Lichtenberg et al. (2021) introduced a coupled numerical model of the interior and atmosphere to study the evolution of magma ocean planets, modeling a handful of single-species volatile cases. They found that magma ocean lifetime varies depending on outgassed atmospheric composition, with H_2-dominated atmospheres yielding long-lived magma oceans, motivating the primary composition of their numerical cases by previously suggested scenarios of planetary evolution. However, they did not link this to a self-consistent description of redox properties. Here, we update their framework of planetary evolution, coupling planetary internal processes to climatic and stellar evolution of evolving magma ocean planets.

Our one-dimensional column model ("PROTEUS") decomposes the physical system formed by the star and the planet into several components: the interior, the surface, the atmosphere, and the star. The magma ocean is assumed to begin as entirely molten, cooling as energy is lost to space through radiation.

2.1. Interior

2.1.1. Energy Transport

The interior component of the system contains the magma ocean and the core. It is solved using an established 1D model ("SPIDER" - Bower et al. (2018), Bower et al. (2019), Bower et al. (2022)). At each level of pressure p and specific entropy S, the melt fraction is calculated according to

$$\phi = \begin{cases} 1 & \text{if } S > S_l \\ (S - S_s)/(S_l - S_s) & \text{if } S_l \geq S \geq S_s \\ 0 & \text{if } S_s > S \end{cases} \quad (1)$$

where S_l and S_s are the specific entropies of the liquidus and solidus at p. To evolve the interior, SPIDER solves the energy conservation equation in terms of specific entropy,

$$\int_V \rho \tilde{T} \frac{\partial S}{\partial t} dV = -\int_A \tilde{F} dA + \int_V \rho H dV \quad (2)$$

where $\tilde{T}$ is the temperature, ρ is the mass density, $\tilde{F}$ is the net heat flux, and H is the internal heat generation. Positive fluxes are measured in the upward direction. $\tilde{F}$ is the sum of contributions by convection, phase mixing, conduction, and gravitational settling. Heat from the radioactive decay of ^{40}K, ^{232}Th, ^{235}U, and ^{238}U is included. The initial abundances of these radioisotopes are calculated by scaling measured concentrations for modern Earth ($t = 4.55$Gyr) to the system's age of the start of the simulations (Ruedas, 2017; Turcotte & Schubert, 2002). The flux boundary condition used to solve the interior model is placed at the topmost interior node. Time-integration of Equation 2 provides the evolution of the interior's specific entropy, temperature, and melt fraction. The temperature at the top of the interior $\widetilde{T_s}$ is used to set the interior constraint on the surface energy balance (Equation 3). The mantle is initialized on an adiabat with a specific entropy S_0, which corresponds to an initial surface temperature >3000 K such that all cases begin with a "hot start" and then cool over time. The core releases heat over time into the bottom of the mantle; it acts as a reservoir of heat set by its initial temperature, density (10,738 kg m^{-3}), and heat capacity (880 J kg^{-1} K^{-1}). We do not model radiogenic heating in the core, nor thermal boundary layers on either side of the core-mantle boundary. This core cooling model is described further in Bower et al. (2019) and Lichtenberg et al. (2021). Once the base of the mantle reaches the rheological transition, the role of core energetics may become more relevant: during this phase an inner core may begin to crystallize. However, comparatively small changes in the basal temperature of the solid mantle are not the primary focus of this work.

2.1.2. Outgassing

Abundances of volatile elements in the melt and gases in the overlying atmosphere are together set by their solubility and equilibrium chemistry. The total masses of H, C, N, and O in the planet are prescribed at fixed values, and are partitioned into gaseous volatile species (H_2O, CO_2, N_2, CH_4, H_2, and CO) as well as dissolved into the melt. The solubility of these volatiles is calculated from empirical fits which depend on the temperature $\widetilde{T_s}$ and oxygen fugacity fO_2 (Ardia et al., 2013; Armstrong et al., 2015; Dixon & Pan, 1995; Libourel et al., 2003; O'Neill & Eggins, 2002; Sossi et al., 2023). This accounts for the complex speciation and non-ideal behavior of volatiles when they dissolve. The three reactions $CO_2 + 2H_2 \rightleftharpoons CH_4 + O_2$, $2CO_2 \rightleftharpoons 2CO + O_2$, and $2H_2O \rightleftharpoons 2H_2 + O_2$ are assumed to attain thermochemical equilibrium in the atmosphere (Chase, 1998; Schaefer & Fegley, 2017). The requirement of elemental mass conservation is used to solve for the volatile partial pressures at the surface using Newton's method. This construction depends on the C/H elemental ratio (C/H), total hydrogen inventory ($[H]$), and nitrogen concentration x_N as input parameters to set the total amount of the volatile elements (H, C, N, O) in the atmosphere and magma ocean. Adopting estimates of Earth's primitive mantle, the nitrogen concentration x_N is fixed at 2 ppmw relative to the total mantle mass, although this value could vary between planetary systems (Wang et al., 2018).

2.1.3. Magma Ocean Solidification

We assume a chondritic mantle based on the solidus and liquidus in Andrault et al. (2011) and Hamano et al. (2013)—see Bower et al. (2019). Typically, a fully molten mantle with such a composition would freeze out from the bottom to the top, however, even with these assumptions fractional crystallization can induce heterogeneous freeze-out (Bower et al., 2022). This does not account for volatile partitioning into the solid phase. As is a typical assumption in the literature (Abe, 1993; Elkins-Tanton, 2012; Lebrun et al., 2013), we assume that volatiles are homogeneously distributed throughout the melt due to the vigorous convective mixing and stirring from accretion and large impacts. It is possible that mantle convection with large Rayleigh numbers could trap volatile-rich melt within large scale circulations, leading to inhomogeneous volatile distribution and inhibition of outgassing (Salvador et al., 2023; Siggia, 1994). Formation of crystals within the solidifying mantle leads to a significant increase in viscosity as the melt fraction passes through the "rheological transition" (Bower et al., 2022). The characteristic location of this transition—the rheological front—progresses upward during magma ocean solidification. If this occurs rapidly, it could lead to small pockets of melt becoming embedded within the solid part of the mantle, thereby trapping volatiles deep within the planet (Elkins-Tanton, 2012; Hier-Majumder & Hirschmann, 2017; McKenzie, 2011). Together, this means that our outgassing model likely overestimates the amount of volatiles in the atmosphere and therefore the atmospheric surface pressures.

2.2. Model Coupling

It is thought that magma oceans could be covered in a thin conductive boundary layer, which limits heat transport through the surface (V. Solomatov, 2015; Schaefer et al., 2016; Lebrun et al., 2013; Lichtenberg et al., 2021). This boundary layer is analogous to those which form on lava ponds on Earth, but instead occurring on a global or hemispherical scale. This boundary layer is parameterized in our model by a thin layer of constant thermal conductivity κ_c and thickness d_c that conducts a heat flux according to Fourier's law

$$F_c = \kappa_c \frac{\widetilde{T}_s - T_s}{d_c}. \tag{3}$$

This layer acts to couple the top-of-mantle temperature $\widetilde{T}_s$ to the bottom-of-atmosphere temperature T_s. The temperature at the top of the boundary layer (T_s) is less than that at the bottom $\widetilde{T}_s$ (which is fixed by the topmost node of the interior model) for a net positive conductive heat flux F_c. Equation 3 is used to determine the temperature at the base of the atmosphere by ensuring that F_c is equal to the net (up minus down) bolometric radiative flux at the top of the atmosphere, which is calculated as

$$F_t = F_{\text{up}}^{\text{LW}} + F_{\text{up}}^{\text{SW}} - F_{\text{down}}^{\text{LW}} - F_{\text{down}}^{\text{SW}} \tag{4}$$

This model of surface flux balance is adopted because it conserves energy by construction and allows for temperature discontinuities at the surface. The top of atmosphere radiative flux is used instead of the near-surface flux because radiation will be the primary mechanism for energy transport at the top of the atmosphere, as opposed to at deeper levels where convection may dominate. This is consistent with our stratospheric prescription. Schaefer et al. (2016) used a similar model for the parameterization of the boundary layer. The temperature at the bottom of the atmosphere T_s is set by the solution of Equation 3. For a given top-of-mantle temperature $\widetilde{T}_s$ (calculated by SPIDER), T_s is determined by using the secant method to find the root of $F_c - F_t$. F_c is the net upward-directed top-of-atmosphere radiative flux calculated using the radiative transfer code described below. This implementation conserves energy between the atmosphere and interior models, but is not guaranteed to do so locally throughout the atmosphere due to the prescriptive nature of the atmospheric temperature profile (Section 2.3.1). Once the atmospheric fluxes are obtained (Section 2.3.2), F_t is set as the new flux boundary condition at the top of the interior model. This construction allows feedback between the interior and the atmosphere and ensures that energy fluxes are conserved between the components of the model. The flowchart in Figure 1 shows this graphically.

We take $\kappa_c = 2$ W K^{-1} m^{-1} as a characteristic value of thermal conductivity of this conductive boundary layer, although in reality this quantity would depend on the particular physical and mineralogical properties of the material (Balkan et al., 2017; Chibati et al., 2022). Previous studies have shown that the thickness of this layer is

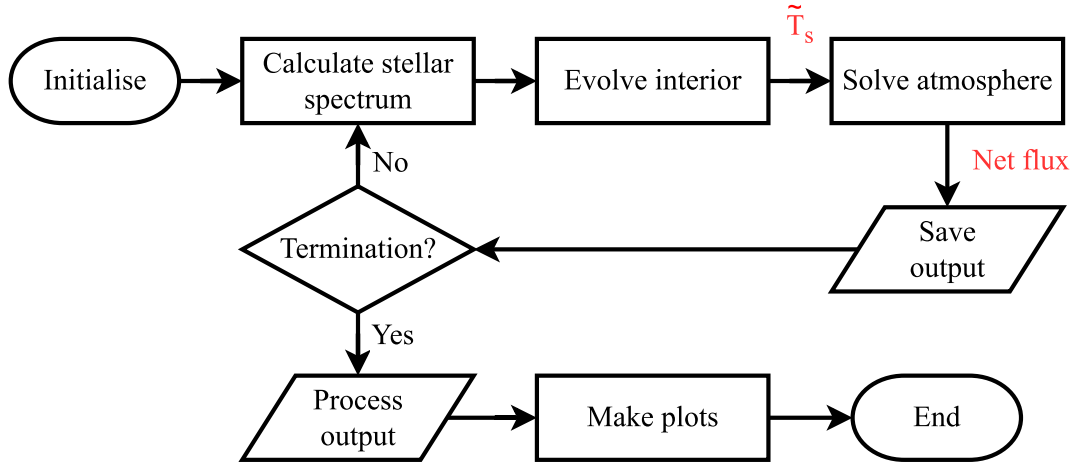

Figure 1. Flowchart outlining our scheme for planetary evolution. The model is initialized into a fully molten state, with the interior and atmosphere coupled together to enable heat transport from the interior into space. At each time-step, the spectral stellar flux impinging on the top of the atmosphere is updated consistently with stellar evolution models, and a check is made for whether Equation 9 or Equations 10a and 10b are satisfied. The top-of-mantle temperature $\tilde{T}_s$ is calculated by the interior model, subject to the top-of-mantle flux boundary condition derived by the surface conduction (Equation 3) and the outgoing radiation from the top of the atmosphere F_t (Equation 4).

important for determining the cooling timescale (Monteux et al., 2016). Observations and models of lava ponds indicate that d_c varies from ∼cm to ∼m depending on temperature contrast and flow speed (Aufaristama et al., 2018; Neri, 1998). Lids on lava ponds are not fully analogous to global magma oceans as the latter cases lack the structural support afforded by the walls of the pools, potentially yielding comparatively smaller d_c (Elkins-Tanton, 2012). Modeling by Lebrun et al. (2013) found that d_c varies between ∼mm and ∼m during magma ocean crystallization, until the rheological front reaches the surface, at which point the thickness of the conductive boundary layer increases to ∼km. It is possible that in the later stages of magma ocean evolution that this thick conductive layer could significantly inhibit further cooling. However, it could be destabilized by dynamical stresses on its bottom boundary and impacts on its top boundary (Elkins-Tanton, 2012). The thickness d_c of this layer is set to a constant characteristic value of 1 cm in this work.

2.3. Atmosphere

2.3.1. Temperature Profile

The atmosphere plays a key role in determining the rate of cooling of the planet's interior, as thermal emission from the surface will be partially or entirely balanced by downward radiation from the atmosphere and the host star. The composition of our model atmosphere is set by the outgassing calculation described in Section 2.1. We assume that the atmosphere is convective from the planet's surface, in line with previous magma ocean studies (Barth et al., 2021; Hamano et al., 2015; Kopparapu et al., 2013; Lichtenberg et al., 2021). Our atmosphere model ("JANUS") implements the multicomponent non-dilute pseudoadiabat of Graham et al. (2021) by integrating dT/dp from the surface $(p = p_s)$ upwards to p $= 10^{-5}$ bar. In regions where all species are in their gas phase, dT/dp is set by the dry adiabat (Equation 5).

$$\frac{dT}{dp} = \frac{1}{c_p(T)} \frac{RT}{p\mu} \tag{5}$$

Moist convection occurs at levels in the atmosphere where any volatile s becomes saturated, which corresponds with a decrease in its mixing ratio. Saturation is defined according to the Clausius-Clapeyron equation. It is assumed that all condensates are instantaneously rained-out and then re-evaporated within dry regions at higher pressures.

Table 1
Sources of Line-Absorption, Literature References, and Corresponding Collisional Absorption Pairings

Gas	References	Collisional pairings
H_2O	POKAZATEL—Polyansky et al. (2018)	H_2O, N_2
H_2	RACPPK—Roueff et al. (2019)	H_2, CH_4, CO_2, N_2
N_2	WCCRMT—Western et al. (2018), Western (2017), Barklem and Collet (2016), Shemansky (1969)	N_2, H_2, H_2O
CO_2	UCL-4000—Yurchenko and Tennyson (2020)	CO_2, H_2, CH_4
CH_4	YT34to10—Yurchenko and Tennyson (2014), Yurchenko and Waldmann (2017)	CO_2, H_2
CO	HITEMP2019—Li et al. (2015)	None

Note. Absorption from the water self-continuum is calculated using Version 3.2 of the MT_CKD model (Mlawer et al., 2012, 2023). All other collisional absorption is calculated using the HITRAN collisional absorption database (Karman et al., 2019). The DACE opacity database derives cross-sections using HELIOS-K (Grimm et al., 2021).

The gravitational acceleration g and heights z of each level are obtained by simultaneously solving for hydrostatic equilibrium (using the ideal gas equation of state) and Newton's law of universal gravitation; an Euler method is used to integrate these equations from the surface upward. Mean molecular weight μ [kg mol^{-1}] and specific heat capacity at constant pressure $c_p(T)$ [J K^{-1} mol^{-1}] are obtained from the well-mixed composition and NIST data.

2.3.2. Radiative Transfer

The SOCRATES radiative transfer code—developed by the UK Met Office—is used to solve the plane parallel two-stream radiative transfer equation (Edwards & Slingo, 1996; Sergeev et al., 2023; Walters et al., 2019). We include gaseous absorption, collisional absorption, and Rayleigh scattering of longwave and shortwave radiation. The exponential sum fitting correlated-k approximation is used for determining the opacity of the gas mixture at each level, depending on its pressure and temperature (Amundsen et al., 2014, 2017). Combined gaseous absorption is treated using the random overlap method (Goody & Yung, 1989; Lacis & Oinas, 1991). The flexibility afforded by random overlap (with resorting and rebinning of k-terms) can yield smaller errors compared to a reasonably sized pre-mixed k-table (Amundsen et al., 2017). The k-coefficients are fitted with the number of terms in each band selected such that the root-mean-squared transmission error across each band is less than 1%. The transmission error is calculated as the difference between the exact transmissions (from the opacity tables) and that calculated using the fitted k-terms and weights.

We initially calculate k-coefficients directly from the HITRAN2020 database using 318 spectral bands between 0 and 30,000 cm^{-1} for comparison with previous work (Gordon et al., 2022). We also calculate k-coefficients using absorption cross-sections from the University of Geneva's Data and Analysis Center for Exoplanets (DACE) opacity database, tabulated at 80 pressure points (−6 to +3 log bar), 18 temperature points (100–2895 K), and 256 bands (1–35,000 cm^{-1}). This makes our opacity calculations much more complete than previous work; Kopparapu et al. (2013) for example, tabulated absorption to a maximum temperature of 600 K using 55 bands between 0 and 15,000 cm^{-1}, and Selsis et al. (2023) used 66 spectral bands. Lower transmittances and net fluxes are therefore expected when using the DACE-derived data as it includes more lines (particularly in the optical/UV regimes and at high temperatures). Table 1 outlines the included absorbers, their literature sources, and corresponding collisional pairings.

The downward shortwave flux (absorbed stellar flux - ASF) at the top of the atmosphere is calculated as

$$F_{\mathrm{ASF}} = F_{\star} f_s (1 - \alpha_b) \cos(\theta) \tag{6}$$

where θ is the solar zenith angle, f_s is a scale factor associated with the axial rotation of the planet, α_b captures additional contributions to the planetary albedo, and $F_{\star}$ is the instellation flux (Section 2.4). In all cases modeled in this work there is an asynchronous relationship between the planet's orbital period and their day length, so we set $\theta = 48.19°$ and $f_s = 3/8$ (Cronin, 2014). We do not model the impact of clouds on the radiative transfer, so we set $\alpha_b = 0$ in all calculations to represent a sky clear of aerosols. Note that α_b does not represent the bond

albedo, as Rayleigh scattering and surface reflectivity are modeled as separate and distinct processes. The instellation is calculated as

$$F_\star = \frac{L_\star(t_\star)}{4\pi a^2} \tag{7}$$

where $L_\star(t_\star)$ is the stellar luminosity at age $t_\star$, and a is the orbital separation.

Upwelling longwave radiation from the surface of the planet is set by blackbody emission at a temperature $T = T_s$. The surface albedo α_s cannot be tightly constrained due to a lack of experimental data on molten surfaces, however Essack et al. (2020) conclude that molten silicate surfaces have a low reflectivity, so we set α_s to 0.1 in all of our simulations.

2.3.3. Stratosphere

The assumption that these atmospheres are entirely convective has been challenged. Selsis et al. (2023) demonstrated that pure-steam atmospheres in global radiative equilibrium may form radiative layers near the surface, which decreases the surface temperature (for a given net flux) compared to a fully convective atmosphere. It is as-yet unclear how much this extends to atmospheres of more complex composition, and to atmospheres which start in an initially molten and cooling-off state as in this work. Solving for a radiative-convective temperature profile is beyond the scope of this work, but we can make an approximation of a radiative stratosphere—which is assumed to be transparent to shortwave radiation but a gray absorber of longwave radiation—by imposing $T(p) \geq T_r$, where

$$T_r = \left(\frac{(1-\alpha_b) f_s F_\star}{2\sigma_{\rm SB}}\right)^{1/4} \tag{8}$$

is the radiative skin temperature of the planet, set by the bolometric stellar flux $F_\star$ and the bond albedo (R. T. Pierrehumbert, 2010). $\sigma_{\rm SB}$ is the Stefan-Boltzmann constant. This prescription of an isothermal stratosphere does not address the possibility of near-surface radiative layers. We assess whether or not convection shuts off in Section 3.6 by analyzing radiative heating rates throughout the atmospheres of two case studies.

2.4. Star

Flux from the host star factors into the evolution of the planet through its radiative energy balance. A star's luminosity evolves both bolometrically and spectrally over time depending on its spectral class and angular momentum endowment—see Figures 5 and 11 of Johnstone et al. (2021)—which can impact both the climate and chemistry of orbiting planets (Tsai et al., 2021; R. T. Pierrehumbert, 2010). We use the model ("MORS") developed by Johnstone et al. (2021) to evolve the stellar spectrum over time self-consistently with the evolution of the orbiting planet. By treating stars as solid shells corotating around solid spheres, MORS models their spin-down sequence and thus obtains X-ray, UV, and bolometric luminosities $L_\star$ based on the angular momentum transport between the two rotating bodies, its age $t_\star$, and known scaling laws from observations and MHD simulations (Johnstone, 2017; Spada et al., 2013). Using a star's modern spectrum as a template (Gueymard, 2004), we then scale the fluxes within these bands in order to obtain an approximation of its historical emission spectrum. The normalized stellar emission spectrum is updated throughout our simulations at intervals of 0.1 Myr while the bolometric flux $F_\star$ is updated every 200 years. For this work, we treat the Sun as an "intermediate" rotator by placing it in the 60th percentile for rotation speed for its mass and age (Gallet & Bouvier, 2013).

2.5. Model Termination

The model terminates under two possible phase states at the end of the simulation. This occurs either when the planet has solidified (where the global melt fraction Φ is less than a critical value)

$$\Phi < 0.005, \tag{9}$$

Table 2
Parameter Axes Used to Construct Our Grid of Models

Parameter	Symbol	Points	Range or values
Orbital separation	a	7	0.105, 0.316, 0.527, 0.737, 1.054, 2.108, 3.162
Oxygen fugacity	fO_2	7	−5, −3, −1, 0, 1, 3, 5
C/H ratio	C/H	7	0.01 to 2.0 logarithmically spaced
Total H inventory	[H]	3	1, 5, 10

Note. There are 1,029 grid points in total. Orbital separation is measured in AU from the Sun (Equations 6 and 7 in Section 2.3.2). The other three parameters relate to the outgassing (Section 2.1.2) of volatiles: oxygen fugacity fO_2 is measured in $\log_{10}$ units relative to the Iron-Wüstite (IW) buffer, C/H is the ratio of the total mass of carbon to the total mass of hydrogen in the mantle and atmosphere combined, the total hydrogen inventory $[H]$ is measured in units of the total amount of hydrogen in all of Earth's oceans (hereafter abbreviated to "oceans").

or when the planet enters into a steady state (where the global melt fraction is unchanging and the net radiative flux F_t is small—cf. Equation 4).

$$|d\Phi/dt| < 10^{-10}\mathrm{yr}^{-1} \tag{10a}$$

$$F_t < 0.8\mathrm{Wm}^{-2} \tag{10b}$$

This means that the lowest possible surface temperature in our model is set by the solidus temperature of the mantle. As a result, the surface temperatures are always supercritical and no oceans are formed upon rainout. It is possible that these planets would continue to cool post-solidification, and potentially form liquid oceans above a solidified mantle. Figure 1 outlines the coupling process by which the components of the system are able to interact. The following subsections outline each component in detail.

2.6. Experimental Configuration

We run our model across a grid of parameters to explore their impact on the composition of the atmosphere, the phase state at model termination (i.e., a solid or molten mantle), and the duration of the rapid cooling stage. The grid is configured according to the parameters in Table 2. All cases set $M_p = M_\oplus$, $R_p = R_\oplus$, and $R_{\mathrm{core}} = 0.55R_p$.

The range of a bounds the habitable zone (roughly 0.95 to 2.4 AU) and extends to small separations for applicability to Venus and highly irradiated exoplanets (Kasting et al., 1993; Ramirez & Kaltenegger, 2017). Bulk elemental endowment depends on the location and timing of planetary formation (Drażkowska et al., 2023; Krijt et al., 2023), so we use a broad range of $[H]$ and C/H which encompass concordant estimates for primitive Earth (Wang et al., 2018). Mineralogical variations alone will introduce a range of at least 4 log units to fO_2 (Guimond et al., 2023), however, inferences of the redox state of material accreted onto white dwarf stars indicates an oxygen fugacity comparable to asteroids within the solar system (Doyle, Klein, et al., 2019; Doyle, Young, et al., 2019). Constraints on Mars' redox state derived from measurements of martian meteorites imply a variation of at least 3 log units (Wadhwa, 2001). Observations of Mercury's surface by the MESSENGER spacecraft have been used to infer a highly reduced composition (Cartier & Wood, 2019). We therefore explore a range of fO_2 from extremely reduced to oxidized.

3. Results

3.1. Model Validation

A key requirement is that our atmosphere model is able to reproduce the runaway greenhouse effect of a pure-steam convective atmosphere. The temperature structures of our model atmospheres are directly tied to the surface temperatures and pressures; each layer can be in one of three states: on the dry adiabat, on a moist pseudoadiabat, or isothermal if above the tropopause. For sufficiently large T_s, most of the atmosphere will lie on the dry adiabat (Equation 5). At cooler T_s, some fraction of the column will be condensing in which $T(p)$ is set only by the condensing gas through the Clausius-Clapeyron relation. Therefore, the outgoing longwave radiation (OLR) becomes decoupled from T_s in cases where the effective photosphere is within a condensing region,

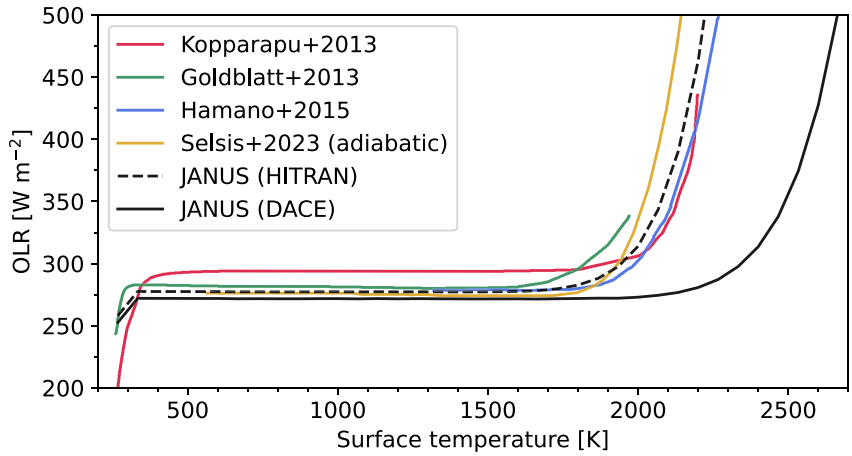

Figure 2. Outgoing longwave radiation (OLR) versus surface temperature for thick pure-steam atmospheres. JANUS is compared against curves from Hamano et al. (2015), Goldblatt et al. (2013), Kopparapu et al. (2013), and Selsis et al. (2023). Taking the value at 1,400 K, we find a runaway OLR limit of 277 W m^{-2} using HITRAN-derived opacities (dashed black line), which is close to the canonical Simpson-Nakajima limit of 280 W m^{-2} (Komabayasi, 1967). The solid black line plots values calculated with JANUS using DACE-derived opacities, which yields an OLR limit of 272 W m^{-2}. With the most complete absorption data, the post-runaway transition shifts to higher temperatures (∼2100 K as opposed to ∼1800 K).

leading to the so-called "runaway OLR limit." Only when the deep atmosphere (and/or surface) are sufficiently hot can the planet enter into a post-runaway regime, where the photosphere is within a dry convective region which couples T_s to the OLR (Boukrouche et al., 2021; Goldblatt et al., 2013; Innes et al., 2023). Additionally, since emission from the atmosphere and surface is set by the Planck function, hotter temperatures lead to emission at shorter wavelengths, allowing for increased transmission through windows between H_2O absorption features and OLR to increase with T_s(R. T. Pierrehumbert, 2010). This behavior is important because it limits how fast the planet may cool. In order to test the radiative transfer, Figure 2 plots OLR versus surface temperature. JANUS is demonstrated to compare well against previous studies when calculating fluxes using the HITRAN-derived opacities. Due to increased line absorption below 500 nm, the calculations using DACE-derived (POKAZATEL Version 2) opacities finds a lower OLR limit and a hotter transition into the post-runaway regime. This is because higher T_s are required to emit through the comparatively narrower windows, and increased opacity shifts the photosphere to lower pressures. Lower temperatures yield minimal differences in the flux between the two linelists, because HITRAN is sufficiently complete in this regime.

Given the large difference between the two JANUS cases in Figure 2, we further validate the DACE-derived opacities and our pipeline for processing them. First, we calculate k-coefficients for absorption by pure O_2 gas using opacities from DACE, which are themselves derived from the HITRAN linelist for O_2. There are minimal differences (∼0.16%) in OLR calculations with these k-coefficients compared to when using k-coefficients and opacities calculated from the HITRAN linelist directly (not from DACE). This indicates that our k-coefficients derived from DACE are accurate. When fitting k-coefficients to a tighter tolerance of 0.0005%, there are minimal differences in the OLR (<1 W m^{-2} at 2,800 K). We also perform a sensitivity test on the number of spectral bands by calculating the OLR of a pure-steam atmosphere with $T_s = 2800$ K: compared to calculations with 4096 bands, there is a 1.8% decrease in OLR with 256 bands, a 14.2% decrease with 48 bands, and a 61.7% decrease with 16 bands. This trend can be explained by narrow emission windows being better resolved with more bands (Salvador et al., 2017). Two hundred and fifty-six bands are used for the rest of this work. The continua databases used in this work were developed for use alongside HITRAN, so we also test whether the aforementioned flux differences (between simulations using DACE- or HITRAN-derived opacities) could be attributed to continuum incompatibility with the linelists we used. In line with the predictions of Mlawer et al. (2023), we find that the relative flux differences are present even with the continua disabled, meaning that they can be attributed to differences in line absorption.

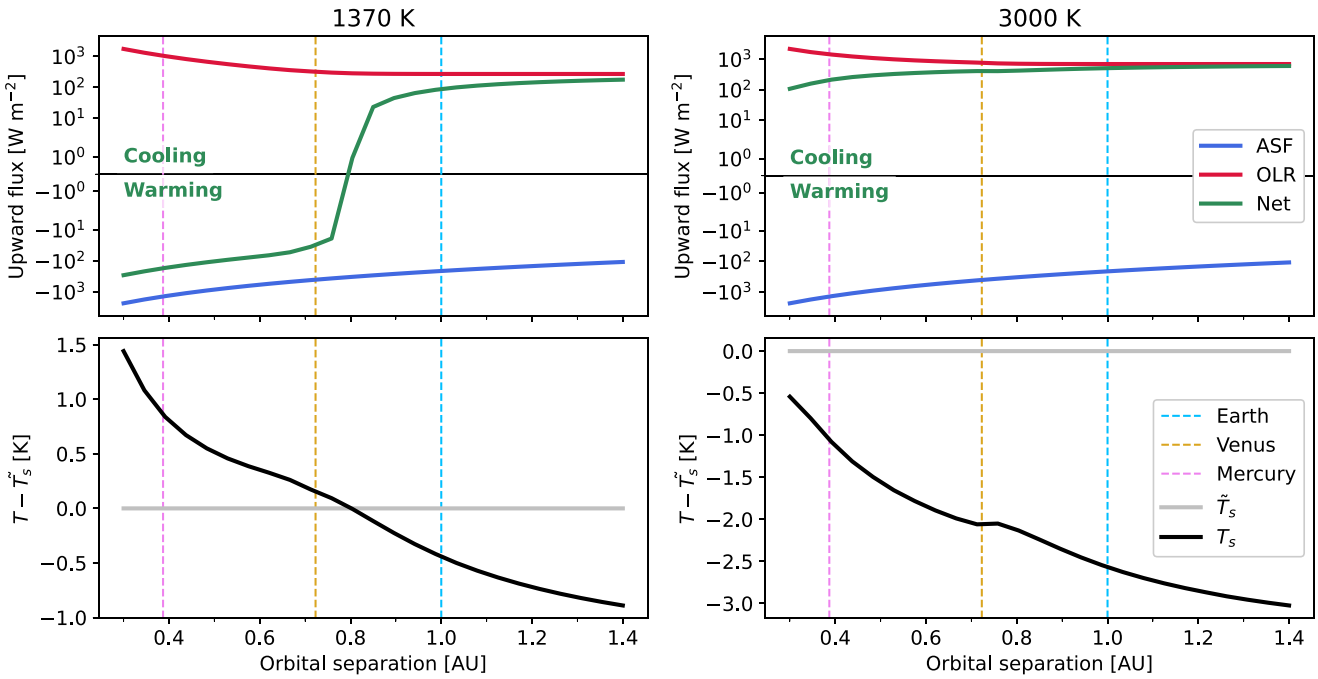

Figure 3. Global energy balance versus orbital separation for two cases of mantle temperature 1,370 K (left) and 3,000 K (right). The top panels plot radiative fluxes versus orbital separation. Absorbed stellar flux is the downward top of atmosphere shortwave radiation flux (Equation 6). Green lines plot the net radiative flux at the top of the atmosphere F_t. The bottom panels show the surface temperatures T_s (black line) required to maintain the fluxes in the upper panels, relative to the mantle temperatures $\widetilde{T}_s$ (gray line).

Bodies within the solar system provide a ground truth against which to calibrate and test planetary models. One key requirement is that a model of Earth should solidify, while highly irradiated planets should maintain a permanent magma ocean. To this end, we solved for the radiative fluxes across a series of different orbital separations from a young Sun ($t_* = 100$Myr), setting the planet radius and mass to that of Earth, and prescribing a pure-steam atmosphere of 280 bar Figure 3 plots the resultant fluxes for $\widetilde{T}_s = 1370$ K (left, representing a solid mantle from Hamano et al. (2015)) and 3,000 K (right, representing a completely molten mantle). This demonstrates that a model of Earth would cool below the surface solidus even with a thick steam atmosphere in both cases. At Venus' orbital separation with $\widetilde{T}_s = 3000$ K, the planet emits a positive net top of atmosphere flux which indicates that it would also initially cool. Its net negative top of atmosphere flux for $\widetilde{T}_s = 1370$ K indicates that it would reach radiative equilibrium before cooling to that surface temperature, thereby maintaining some amount of melt under a 100 bar steam atmosphere. A planet at Mercury's orbital separation behaves similarly to that at Venus' in both cases, maintaining some level of melt. These behaviors are validated by the knowledge that Earth no longer maintains a magma ocean, and that Venus may have maintained one until a sufficient amount of water had escaped and/or the irradiation from the Sun decreased (Gillmann et al., 2009; Hamano et al., 2013; Salvador et al., 2023). These results demonstrate that—within the given parameters—this formulation for the surface coupling of the interior and atmosphere components of the system behaves reasonably.

The radiative transfer component of our radiative-convective model does not require further validation here, as it has been well tested under a range of conditions (Boukrouche et al., 2021; Innes et al., 2023; Lichtenberg et al., 2021; Sergeev et al., 2023). We also verified that our integration of the hydrostatic, ideal gas, and gravity equations is reasonable. By comparing against data retrieved from Earth-observing satellites, we found that the Euler integrator provides good accuracy using 210 levels (Dudhia, 2017).

3.2. Fiducial Pure-Steam Atmosphere

As a fiducial case, a test planet is initialized as fully molten and endowed with an arbitrary 10 bar pure-steam atmosphere. The total water endowment (equivalent to [H] = 8.5 times that in Earth's oceans) is therefore set

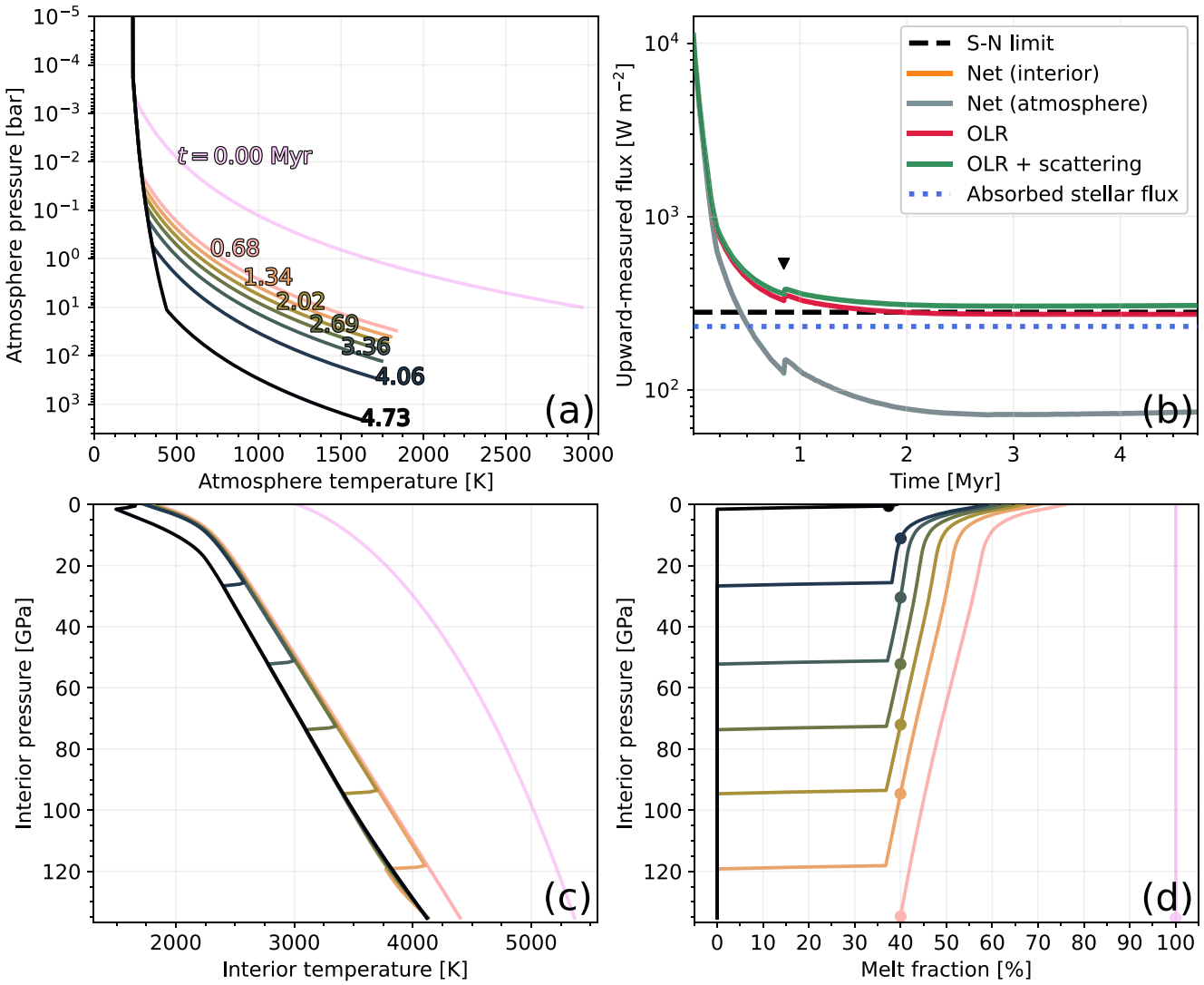

Figure 4. Time evolution of the fiducial model until solidification occurs. Panel (a) atmosphere temperature profiles, with simulation time (Myr) indicated by the colored text on each curve. Panel (b) upward-measured energy fluxes, with the Simpson-Nakajima limit indicated by the dashed black line. Panel (c) interior temperature profiles. Panel (d) interior melt fraction profiles, with the rheological front ($\phi = 40\%$) on each profile indicated by a dot.

by the solubility law and this initial pressure. The planet is placed around a young Sun ($t_* = 100$Myr) at 1 AU. We set $M_p = M_\oplus$, $R_p = R_\oplus$ which approximately represents the configuration of a young Earth.

The surface temperature is initially very large ($T_s = 3023$ K) which places the planet into a post-runaway state that enables large net outgoing fluxes ($F_t = 10.6 \mathrm{kW m^{-2}}$). The planet cools rapidly, resulting in a solidification time of 4.7 Myr. This is too short for significant stellar evolution to occur (Baraffe et al., 2015). Figure 4 shows the evolution of this planet's atmosphere and interior temperatures, energy fluxes, and mantle melt fraction. Panel a shows that the surface temperature of 1,615 K at solidification is within the runaway greenhouse regime indicated by Figure 2 due to the region of deep moist convection between 100 and 0.01 bar. The simulation spends most of its time in the runaway greenhouse regime which limits the OLR to 273 W m^{-2}, which, minus the incoming stellar radiation and the scattering contribution, results in a net outgoing flux of 74 W m^{-2} (panel b). The planet does not attain radiative equilibrium in these simulations because solidification occurs first. The non-zero net upward energy flux at solidification (panel b) indicates that the planet would continue to cool below the surface solidus temperature. The interior cools rapidly from its initial state to below the liquidus (panel c). It then spends a comparatively longer period with a mushy mantle until solidification occurs (panel d). Panel d also

shows the ascent of the rheological front (defined at $\phi = 40\%$ as in Lebrun et al. (2013)), which tracks where the mantle undergoes a rheological transition between dynamics characteristic of a melt to those of a solid (Bower et al., 2022). The black triangle in panel b indicates the time at which the rheological front begins its ascent (cf. panel d), at which point mixed-phase energy transport processes enter into the system.

The gray and orange curves in Figure 4b overlap continuously, demonstrating that our method for loosely coupling the interior and atmosphere components of the model is reasonable. The contribution from Rayleigh scattering is small (34 W m^{-2}) but not insignificant compared to the OLR at solidification. This result is consistent with Section 3.1 in that an Earth-like case solidifies under a pure steam atmosphere. The isothermal stratosphere (235 K) has a small presence although it has little impact on the simulation due to the small opacity at such low pressures.

The solidification time of 4.7 Myr is comparable with the value of 3.9 Myr found by Hamano et al. (2015) for a planet at 1 AU. The 0.8 Myr difference may be reasonably accounted for by different total reservoirs of hydrogen and oxygen compared to our case, different opacities and melting curves, and our inclusion of Rayleigh scattering and non-zero surface albedo. Lebrun et al. (2013) found that magma ocean duration is "quite sensitive" to the planet's H_2O endowment due to the large radiative opacity of H_2O gas. Similarly, Hamano et al. (2015) found that the solidification time of an Earth-like lava planet strongly depends on its initial water inventory, increasing from 0.7 to 630 Myr for 0.1 and 10 oceans respectively (their Figure 4b), the latter case only being able to cool due to atmospheric escape. Lebrun et al. (2013) also found that the magma ocean duration could vary in length by between 0.8 and 2 Myr depending on the choice of mantle solidus and liquidus curves; this factor being particularly important when comparing our results with the literature given that PROTEUS is able to model the magma ocean in 1D. Previous works used parameterized adiabatic mantles, which assume that convection is the only energy transport process (effectively making them zero-dimensional). With these modeling differences under consideration our solidification time is taken to be reasonable. Solidification of the mantle leads to significant outgassing of water, with the surface partial pressure monotonically increasing from 10 to 2054 bar in this simulation.

Solidification is bottom-up, so the surface layer is the last to begin to solidify (Figure 4d). This occurs at 0.2 Myr, at which point crystals are forming within the melt and settling at the bottom of the magma ocean (Bower et al., 2022; V. S. Solomatov & Stevenson, 1993a, 1993b; V. S. Solomatov, 2000). While convection rapidly transports energy upwards ($\sim 10^{10}$ W m^{-2}), this is largely offset by the effective downward transport of energy by latent heat ($\sim -10^{10}$ W m^{-2}). Additionally, gravitational settling acts to transport energy upwards ($\sim -10^{7}$ W m^{-2}). Inclusion of these additional energy transport processes alongside convection reduces the net upward energy transport, and correspondingly increases the magma ocean cooling time. Although we include radiogenic heating for completeness, the simulated global heat flux through the surface of the planet arising from radioactive decay is initially 0.282 W m^{-2} and then decreases by 0.267% over the course of the simulation. This is negligible compared to the other heat transport processes in this case.

3.3. Parameter Exploration

Across our parameter grid of 1,029 cases, 413 (40%) result in complete solidification, while 616 (60%) reach radiative equilibrium and thereby retain permanent magma oceans of various depths. The minimum, median, and maximum times to solidify are 4.0×10^5, 3.0×10^6, and 1.1×10^8 yr respectively. The maximum time for a case to reach radiative equilibrium is 1.4×10^8 yr. Figure 5 plots distribution functions for all cases explored, which statistically represents how four dependent variables (columns) vary according to the four independent variables (rows, Table 2). A broad range of evolution pathways are demonstrated to be possible for a given planet, even at a fixed orbital separation.

The solidification time is sensitive to the orbital separation (panel i), typically decreasing with orbital distance. This is because the incoming stellar flux is smaller at larger distances, so the outgoing flux becomes increasingly dominant in the total energy balance. The solidification time is shortest (median value approx. 3 Myr) at 3 AU, where the planet rapidly cools and solidifies. As demonstrated by the fiducial case, complete solidification leads to significant outgassing (panel j) and large surface pressures. The longest solidification time (approx. 90 Myr) is larger than that found by the fiducial pure-steam case, indicating that the lifetimes of non-permanent magma oceans may be extended by atmospheres of mixed compositions due to the additional sources of opacity. The

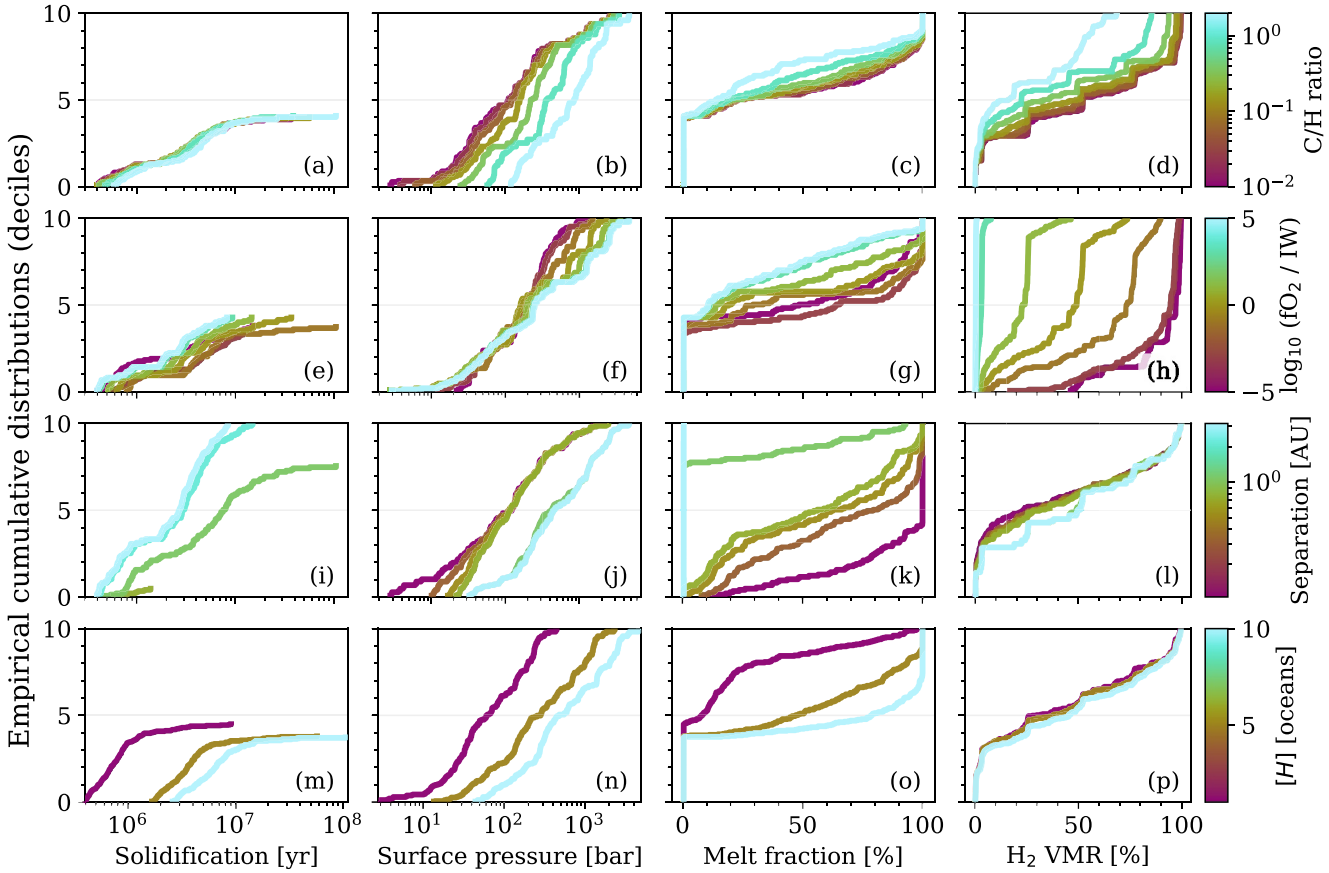

Figure 5. Empirical cumulative distribution functions for four independent variables (colorbars) and four dependent variables (x-axes). Curves are produced for an independent/dependent variable combination (v_i, v_d) by filtering grid cases to each value of v_i (rows), extracting the corresponding v_d (columns) values at model termination, and then sorting the v_d values in ascending order. For a given curve the corresponding v_i is held constant while all other independent variables are allowed to vary, thereby producing the distribution. If a variable v_d has a strong dependence on a variable v_i, then the distributions in the corresponding panel will tend not to overlap. Steep curves (in the $dy/dx > 0$ sense) correspond to v_d being distributed around a small range of values, while shallower curves correspond to a wider distribution. The data are plotted for all four axes of the parameter space (Table 2) and a selection of four dependent variables (solidification time, total surface pressure, interior melt fraction, and H_2 mole fraction). Cases which reach radiative equilibrium are treated as having an infinite solidification time, and thus do not appear explicitly in panels (a, e, i, m).

global melt fraction is directly tied to the orbital separation (panel k) such that less irradiated cases more commonly solidify. Complete solidification only occurs for a small fraction of cases for $a \leq 0.7$ AU (panel i).

Across all cases and times across our grid of simulations, the surface pressure is maximized at 4711 bar by a H_2O- and CO_2-dominated atmosphere produced by a solidified magma ocean after 4.7 Myr of evolution. Some non-solidifying cases attain global radiative equilibrium very slowly due to the imbalance of outgoing and incoming radiation being very small. The most extreme example of this (Case 635) evolved with a thick H_2 dominated atmosphere for 142 Myr before satisfying our criteria for radiative equilibrium (Equations 10a and 10b).

Alongside the orbital separation, the hydrogen inventory of the planet $[H]$ exerts significant control over the solidification time (panel m). The solidification time increases with $[H]$. The oxygen fugacity and C/H ratio have a smaller but non-zero impact on the solidification time (panels a and e). The ensemble-median melt fraction varies from 10% to 80% depending on the value of $[H]$ (panel o). $[H]$ is critical to partially molten cases because speciation of hydrogen atoms into H_2, H_2O, and CH_4 upon outgassing contributes significant radiative opacity to the atmosphere, slowing energy loss to space and thereby prolonging the evolution of the planet and potentially preventing solidification entirely.

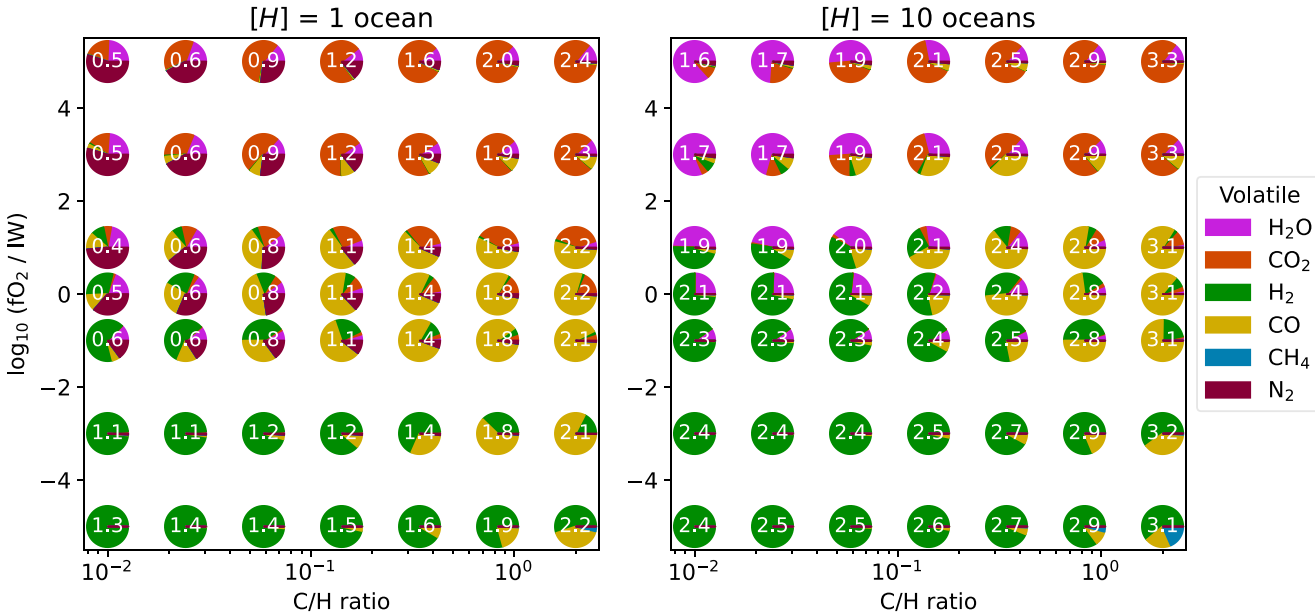

Figure 6. Atmospheric composition for planets which do not solidify. Pie charts display the atm mol fractions χ_i (equivalently, volume mixing ratios $n_i/n_{\text{total}} = p_i/p_{\text{total}}$) for all six included volatiles across the parameter space at 0.1054 AU. The white numbers enumerate the total surface pressure as $\log_{10}(p_s/\text{bar})$, rounded to 1 decimal place. Note that mole fraction is a relative measure of molecule number density, so even at C/H = 2 (a measure of mass ratio) it is possible for there to be more H_2O than CO_2.

There is a large range of H_2 mole fraction across the parameter space (panel h), with it primarily being controlled by the oxygen fugacity of the mantle. H_2 is consistently dilute (maximum mole fraction <5%) under the most oxidizing conditions $(\text{fO}_2 \geq \text{IW} + 3)$, but is consistently dominant (median mole fraction >50%) in reducing cases ($\text{fO}_2 \leq \text{IW} - 1$; see also Figure 6). This is because larger $f\text{O}_2$ promotes the outgassing of oxygen-bearing molecules (such as H_2O) over unoxygenated ones (such as H_2), with variability depending on the gas thermochemistry. Since the model terminates at solidification or radiative equilibrium, surface temperatures always remain high and the abundances of less thermochemically stable reduced species (e.g., CH_4—Chase (1998)) remain small. The production of H_2 dominated atmospheres under reducing conditions are inline with the findings of Schaefer and Fegley (2017) and Ortenzi et al. (2020).

While C/H has only a small impact on the solidification state of the planet (panels a and c), it does yield changes to the total surface pressure (panel b). A large C/H promotes carbon-bearing molecules (such as CO_2) over hydrogenated species (such as H_2, panel d), resulting in significant changes to the mean molecular weight μ of the atmosphere. Surface pressure increases linearly with μ through the hydrostatic equation, yielding higher pressures at larger C/H. This has less impact in solidified cases where outgassing is complete and the total pressure is large, where the atmosphere is typically dominated by steam. Since μ also controls the scale height of the atmosphere, constraints on bulk C/H could be made from observations of permanently molten planets. At the largest C/H the partial pressure of CO_2 approaches 1,800 bar, but H_2O typically remains a dominant or major component of the atmosphere.

Figure 6 explicitly plots the atmospheric composition for highly irradiated planets across two slices of the parameter space (1 ocean and 10 oceans of hydrogen). While the atmospheric composition depends on $f\text{O}_2$ and C/H, $[H]$ exerts the most control over the dominant gas. CO- and CO_2-dominated atmospheres are produced for $\text{C/H} > 0.1$ and $\text{fO}_2 \gtrsim \text{IW} - 1$, inline with Bower et al. (2022) and Sossi et al. (2020). H_2- and CO-dominated atmospheres are common, particularly under reducing conditions, inline with the results of Maurice et al. (2024). The mole fraction of H_2O is typically small across all cases plotted in Figure 6 because it is primarily dissolved into the molten mantles. Methane remains a minor component in all of these cases due to its thermochemical instability and its solubility, with its mixing ratio maximized for the most reducing and hydrogen-rich cases. The low molecular weight of H_2 means that a large partial pressure is required to satisfy the hydrogen mass requirement in cases with large hydrogen inventories, and hence the wide range of cases with H_2 dominated

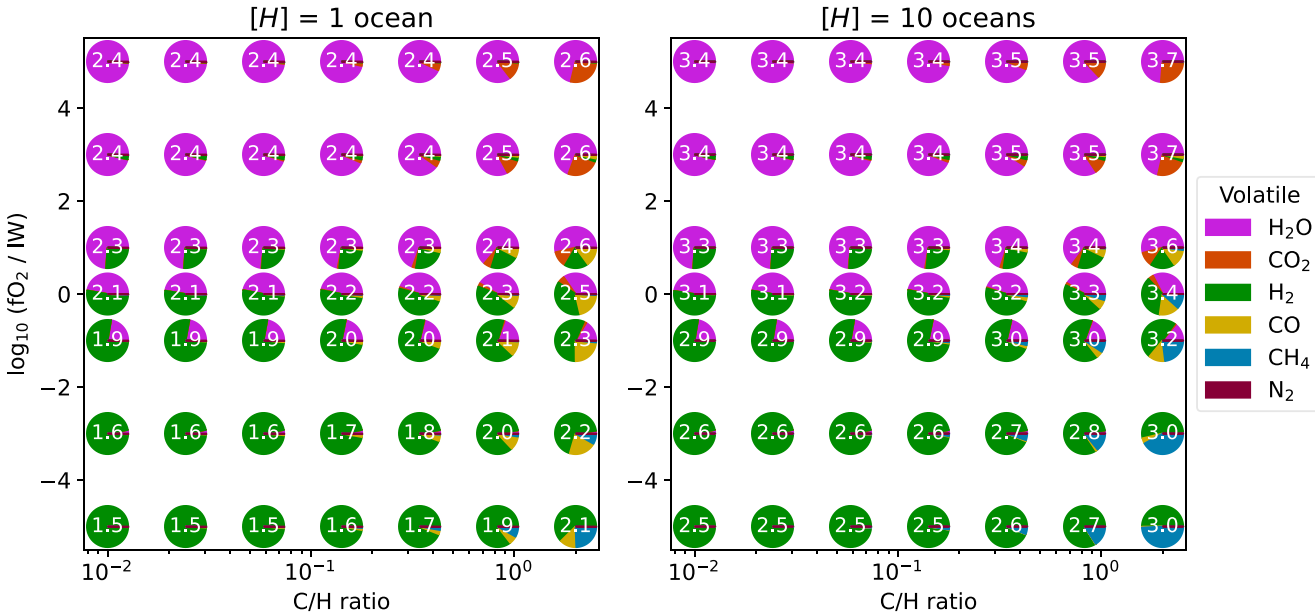

Figure 7. Same as Figure 6, but for cases at 3.162 AU, which are solidified.

atmospheres. The total surface pressure p_s varies by approximately 2 dex in both cases, with larger p_s typically found for larger $[H]$ and C/H. There is a broader range of p_s at oxidizing conditions than at reducing conditions, corresponding to a larger diversity of composition.

Figure 7 plots atmospheric composition for two slices of the parameter space at 3.162 AU, thereby probing the atmospheres of planets which have solidified. The diversity of composition is smaller than for molten cases (Figure 6). This is primarily because the high solubility of hydrogen-bearing volatiles leads to a large fraction of the hydrogen being dissolved in the magma ocean in molten cases, whereas in these cases it is primarily partitioned into the atmosphere because the volume of melt is small. Lower surface temperatures also disfavor the formation of CO, decreasing its abundance relative to CO_2 in these cases. These atmospheres typically have higher surface pressures than in the molten cases of Figure 6 because of the outgassing that occurs with solidification. Because the majority of volatiles have been outgassed, there is a much smaller range of P_s in these cases, which instead set primarily by $[H]$, fO_2, and C/H and not the variable melt fraction.

3.4. Dihydrogen and Water

Figure 5 shows that the total hydrogen inventory and redox state of a magma ocean planet exerts control over its evolution but does not explain the mechanism behind this relationship. Vibrational modes within triatomic H_2O and collisional absorption of H_2 make both of these molecules effective greenhouse gases (Abel et al., 2011; Borysow & Frommhold, 1991; Chen et al., 2011; R. T. Pierrehumbert, 2010; R. Pierrehumbert & Gaidos, 2011). Similarly, Nikolaou et al. (2019) and Katyal et al. (2019) found that planetary volatile endowment is linked to magma ocean cooling and spectral response through outgassing of greenhouse gases. Figure 8 plots the mole fractions of H_2 and H_2O for cases at 1.054 AU, thereby probing the parameter subspace where either solidification or radiative equilibrium outcomes are probable. All cases solidify for $[H] = 1$ oceans, independent of the oxygen fugacity and C/H ratio (left panels). The top-right panel shows that molten cases have an increased mole fraction of H_2, affirming the indications of Figure 5 that the H_2 greenhouse effect is key to preventing/slowing planetary solidification.

For $[H] = 10$ oceans the phase state is more sensitive to C/H and fO_2, although comparison of the two columns indicates that $[H]$ still exerts the most control over the planet's phase state (at 1.054 AU). Cases more oxidizing than Iron-Wüstite always solidify, while more reducing cases are then subject to the planet's C/H ratio. An oxidation state comparable to modern Earth ($\sim$IW+4) falls within the solidifying regime for all cases of $[H]$

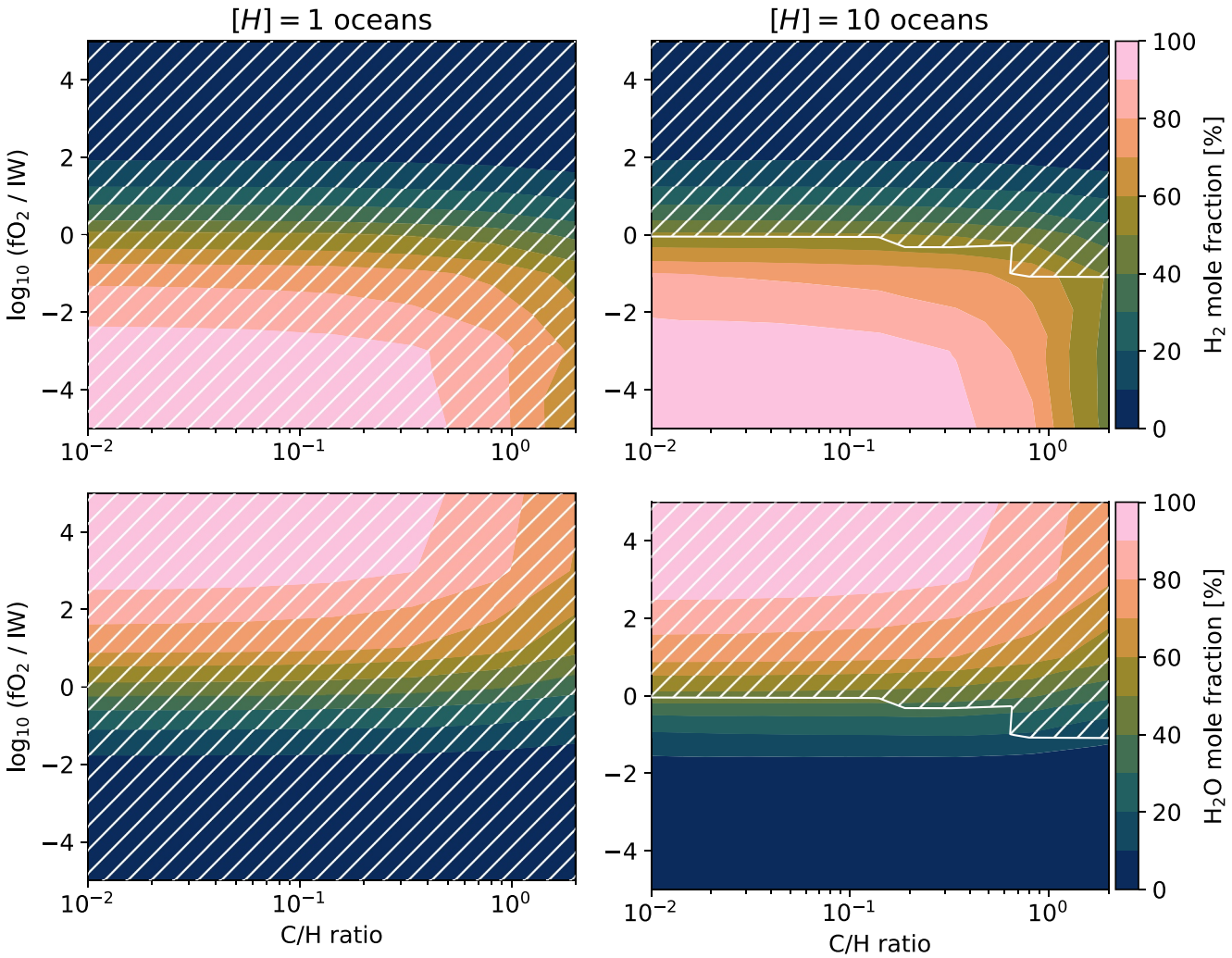

Figure 8. Mole fractions of H_2 and H_2O (rows) plotted versus oxygen fugacity (y-axes) and C/H (x-axes), for two values of planetary hydrogen inventory $[H]$ (columns). The white hatched regions indicate fully solidified cases. Separations of 1.054 AU.

explored in this work; geological evidence suggests that Earth's mantle has been oxidized since at least 3.9 Ga (Nicklas et al., 2018; Rollinson et al., 2017).

The cases at a Venus-like orbital separation of ∼0.737 AU (not plotted in Figure 8) vary between fully molten and mostly solidified. At this distance the models typically enter into a protracted mushy state following rapid initial solidification, which compares well with previous studies (e.g., Lebrun et al., 2013). Early Venus probably produced at least 2 oceans of H_2O from captured nebular H_2, placing $[H] \geq 2$ oceans and ruling out our $[H] = 1$ oceans case (Lammer et al., 2020; Salvador et al., 2023). Assuming that H capture is a viable avenue of water delivery to the young planet, at least 8 oceans of H_2O are expected to have been produced if Venus formed before protoplanetary disk dispersal (Kimura & Ikoma, 2020; Salvador et al., 2023; Williams & Mukhopadhyay, 2019). However, geochemical evidence, such as the present-day D/H ratio of ocean water, suggest substantial uncertainty in these estimates (Broadley et al., 2022). This leaves our $[H] = 10$ oceans case, which requires highly oxidizing conditions (≥IW + 5) and sufficiently low metallicities (C/H > 0.5) in order to avoid large amounts of remnant melt. This case (number 587) terminates within a pseudo-runaway greenhouse regime (OLR = 364 W m^{-2}) with a thick ($P_s = 2472$ bar) CO_2 dominated atmosphere which contains large amounts of steam (H_2O mole fraction of 31%). The high surface temperature ($T_s = 1740$ K) could cause most of the H_2O to

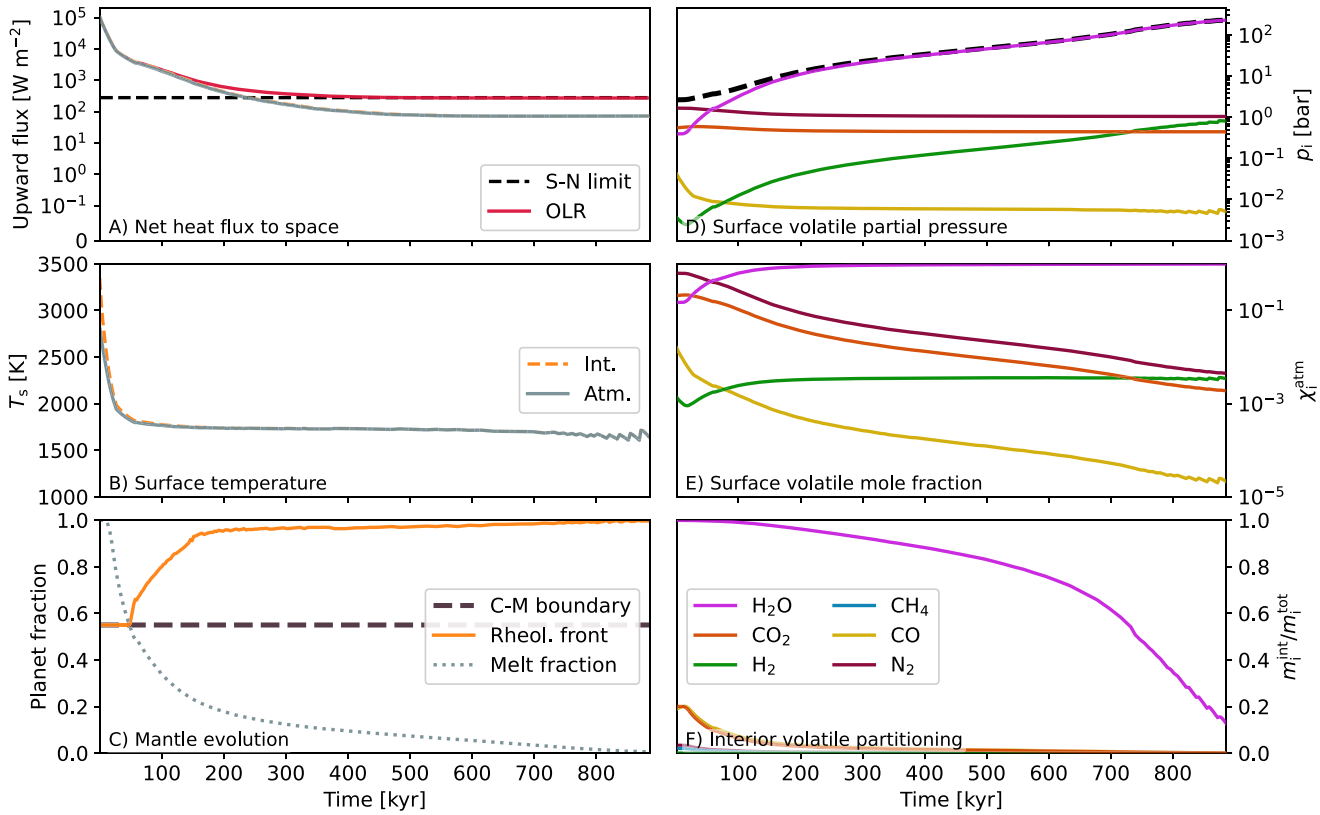

Figure 9. Time evolution of Case 714 (a = 1.054 AU, fO_2 = IW + 5, C/H = 0.01, $[H]$ = 1.0). This corresponds the upper-left corner of the left-column panels of Figure 8, deep within the solidifying region of the grid. All panels share the same x-axis. The top left panel plots the interior (orange line) and atmospheric (gray line) net heat fluxes alongside the outgoing longwave radiation. "C-M boundary" plots the location of the core-mantle boundary ($0.55R_p$) as a baseline for the rheological front. The melt fraction is expressed as a fraction of the mantle—panel c does not imply that the melt fraction of the core is evolving with time in these simulations.

escape during continued evolution, allowing the planet to desiccate and thereby replicate modern Venus-like conditions (Salvador et al., 2023).

3.5. Shallow Magma Oceans

Since the models do not evolve past the point of solidification, surface temperatures do not cool below the surface solidus temperature. Across fully solidified cases, final net top of atmosphere fluxes range between approximate radiative equilibrium (3 W m^{-2}) and rapid energy loss (259 W m^{-2}). Cooling could allow for rainout of some volatile components, reducing the optical depth of the atmosphere.

The initial gas chemical and dissolution equilibrium can yield relatively transparent atmospheres, enabling large net top of atmosphere fluxes and rapid cooling. These atmospheres contain little H_2O as it is dissolved in the magma, and in some cases, such as Case 714 below, are N_2 dominated. Self-regulation then occurs, with H_2O (and other volatiles) being outgassed due to bottom-up crystallization of the mantle, which increases the radiative opacity of the atmosphere. This means that the majority of the interior typically crystallizes rapidly until the optical depth of the atmosphere becomes large enough to stall—or prevent, in radiative equilibrium cases—solidification. One example of this behavior is Case 714; Figure 9 plots the evolution of the planet in this case. Solidification starts from the bottom, with crystals forming at the core-mantle boundary and then at successively shallower layers as the magma ocean cools. The rheological front lifts off the core-mantle boundary at 48.9 kyr and exceeds $0.95R_p$ by 185.0 kyr (Figure 9c). Crystallization first occurs at the top-most layer after 26.7 kyr of evolution, so the magma ocean spends very little time in a completely liquid state, instead spending a significant period of the time with a shallow mixed-phase magma ocean.

Outgassing of H_2O is sufficient to shift the atmosphere from an N_2 dominated composition into a H_2O dominated one (panel e). This also leads to increased abundances of H_2 in the atmosphere through equilibrium chemistry. The radiative opacity of the atmosphere keeps the planet in a runaway regime ($T_s \sim 1700$ K, panels b), with the OLR approximately equal to the Simpson-Nakajima limit (panel a) until solidification. The timescales of CO_2 and CO outgassing are shorter compared to H_2O due to their lower solubility in the mantle. Case 714 would continue to cool post-solidification, since the simulations terminates with a net positive top of atmosphere flux of 72.6 W m^{-2} (Figure 9a). This case could remain within the runaway greenhouse regime for some period of time until the surface cools to a sufficiently low temperature (Figure 2).

During the final stages of solidification ($\Phi < 1\%$) the shallow magma ocean near the surface exhibits non-linear variability on a short timescale of $\approx$ 18kyr, causing the surface temperature oscillate between 1,640 and 1,700 K (panel b) and outgassing to repeatedly pause and resume (panel f) due to the changing melt fraction. As the average melt fraction of the upper layers decreases, convection in the magma ocean becomes sluggish leading to inefficient upward energy transport. This traps heat energy below the surface. The local temperature increases as energy accumulates, eventually re-melting the layer and allowing convection to resume, cooling then continues once more. Volatiles are outgassed during the crystallizing part of this cycle. This behavior is common to cases that fully solidify among our grid of 1,029 models.

3.6. Convective Instability in the Atmosphere

Like most previous works, our atmosphere model uses a prescribed temperature structure where convection is assumed to be the primary energy transport process in the atmosphere (Hamano et al., 2015; Kopparapu et al., 2013; Lichtenberg et al., 2021). However, in the case of pure steam atmospheres in equilibrium with incident stellar radiation, Selsis et al. (2023) showed that convection typically shuts down in the lower portions of thick atmospheres, because there is insufficient stellar flux penetrating to the surface to drive the atmosphere superadiabatic. These atmospheres develop a nearly isothermal layer near the planet's surface, similar to isothermal layers that appear in the analytic gray gas solution (Guillot, 2010; Robinson & Catling, 2012; R. T. Pierrehumbert, 2010). The results are subject to uncertainties in water vapor opacities at high pressure and temperature, but nonetheless require that the shutdown of convection be considered as a possibility. When shutdown of convection in the lower atmosphere occurs, the surface temperature becomes lower than it would be on an adiabat. Selsis et al. (2023) did not consider the case of cooling of a primordial magma ocean, but in the context of a time-dependent calculation, convective shutdown would manifest itself as the lower atmosphere continuing to cool to temperatures below the adiabat, even after the top of atmosphere energy budget comes into balance. This could lead to earlier solidification of a magma ocean than the adiabatic calculations predict, or could lead to solidification of magma oceans predicted to be permanent on the basis of a fully convective atmosphere. In addition to considering the transient case where an initial magma ocean can provide sufficient flux to maintain convection, the configuration we treat differs from Selsis et al. (2023) in that we incorporate additional opacity sources that can block water vapor window regions and help maintain convection.

Ultimately, the possibility of convective shutdown needs to be addressed in a radiative convective model that allows for radiative layers to appear, by means of time-stepping the temperature profile or using a solver that finds atmospheric equilibria without assuming an adiabat. We will consider this point in a future study. As a preliminary indication of convective shutdown, we can test whether the adiabatic profile can be maintained by convection using a variant of the test employed in (Selsis et al., 2023), which involves looking at vertical profiles of radiative heating (or equivalently net radiative flux) for an assumed adiabatic profile. Specifically, we can test whether or not our computed atmospheres would be unstable to convection by analyzing the radiative heating rates of each layer ($H = (g/c_p)\,dF/dP$). Radiative heating at deeper levels and cooling at adjacent upper levels would act to increase the lapse rate and promote convective instability, while the inverse configuration would act to decrease the lapse rate and lead to a convectively stable region. Figure 10 plots per-level radiative heating rates versus pressure, over time, for two of the cases explored in this work. The "Tropopause" marked in the figure indicates the boundary of the idealized isothermal stratosphere assumed in these calculations, whereas actual radiative equilibrium would in most cases yield non-isothermal stratospheres and shift the tropopause level. The left panel indicates that Case 714 initially maintains strong convection from the surface due to the large surface temperature, but a radiative layer may be present at lower pressures ($p < 0.1$ bar). At solidification, Case 714 may not maintain convection from the surface due a small amount of radiative heating near 0.5 bar, although greater heating at lower pressures (0.01 bar) could trigger convection aloft. The center panel indicates that Case 205

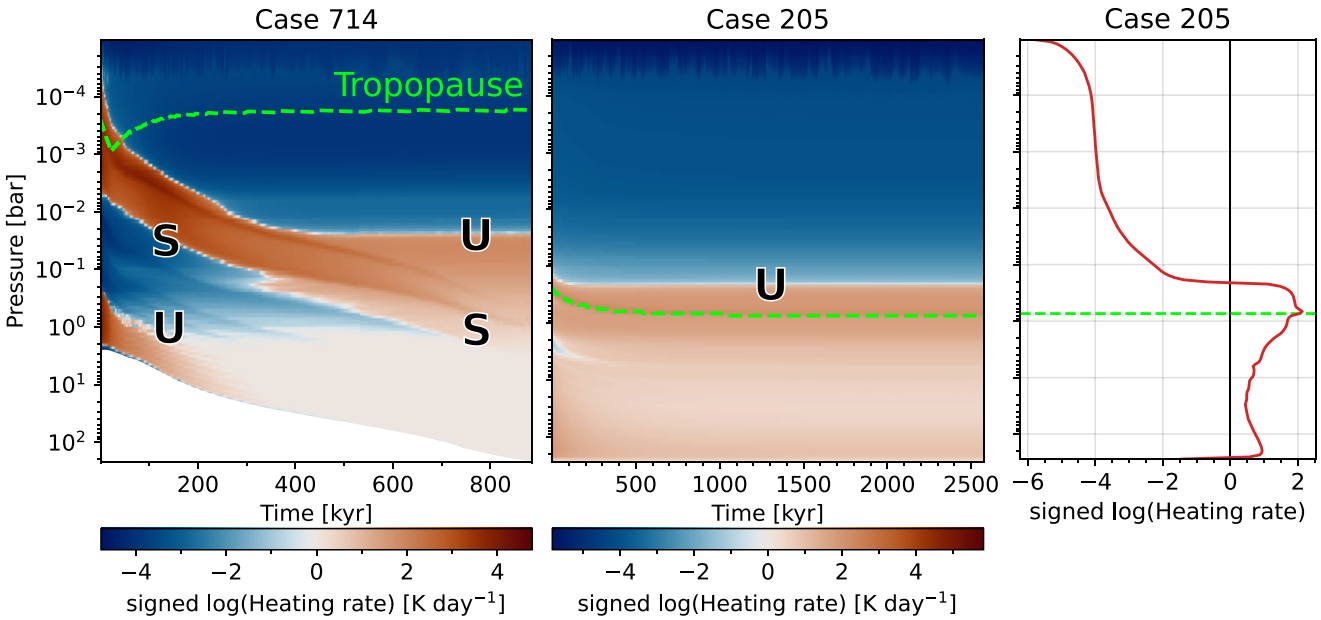

Figure 10. Radiative heating rate versus pressure and time. Case 714 (left) fully solidifies, and was discussed in Section 3.5. Case 205 (center) reaches global radiative equilibrium while maintaining a significant melt fraction of 97.6% under a CO- and H_2-dominated atmosphere. The dashed green lines indicate the tropopause. Regions of relative radiative heating and cooling are labeled "U" and "S," corresponding to whether or not they are unstable or stable to convection. The rightmost panel plots the radiative heating profile at the final timestep of Case 205.

($a = 0.316$AU, $fO_2 = \text{IW} - 1$, $C/H = 0.83$, $[H] = 5$) remains convectively unstable near the surface and above the nominal tropopause throughout the simulation, including when it reaches global radiative equilibrium (rightmost panel). This suggests that the presence of additional opacity sources (in this case, primarily 205 bar of CO and 57 of H_2) may allow a permanent magma ocean to exist, though the suggestion must eventually be tested with more general radiative-convective equilibrium calculations. The right panel shows the radiative heating rate profile for the final timestep of Case 205 (middle panel): we can see that while convection is maintained near the surface and above the tropopause, the layer between roughly 10 bars and 1 bar tends to be stabilized by the heating profile. The resulting stable layer will be eroded by convection below and above, but whether the remaining stable sub-adiabatic lapse rate layer is sufficient to cause solidification must await tests with a full radiative-convective model.

4. Discussion

4.1. Implications

From these trends, we highlight a hierarchy of parameters to which the magma ocean evolution is sensitive. Orbital separation is the most important factor, followed by total hydrogen inventory, mantle oxygen fugacity, and finally the C/H ratio. It is possible that other factors not explored in this work would fit within this hierarchy:

- Surface gravity. For hydrostatically supported atmospheres, surface pressure is proportional to surface gravity; so denser planets may have thicker atmospheres which are maintained against escape.
- Cloud parameterization. Formation of water clouds would reflect stellar flux and also induce additional greenhouse forcing, modulating the rate at which energy is escapes the planet.
- Stellar spectral class and age. Both of these factors can lead to variations in stellar bolometric emission, which directly impacts the planet's energy loss. Similarly, spectroscopic differences between stellar classes could impact cooling depending on the composition of the planet's atmosphere.
- Core size. This is directly tied to the volume of the mantle, and therefore the dissolved volatile inventory, surface pressure, and corresponding optical depth.

There is therefore potential for a very wide range of atmospheric compositions on lava planets, beyond even that exhibited by our modeling. We find that atmospheres on molten planets typically have a more diverse

composition than on solidified planets (which are typically composed of H_2 and/or H_2O at the end of our simulations). Additional post-solidification processes such as weathering may complicate this picture, but this remains applicable for young planets, such as TOI 1807 b and HD 63433 d (Capistrant et al., 2024; Hedges et al., 2021). Telescope observations which constrain atmospheric composition of short-period planets could therefore be used to probe the interior properties and solidification regime of exoplanets. Recent observations by Hu et al. (2024) indicate a carbon-rich CO_2-CO atmosphere on the ultra-short period planet 55 Cancri e, which corresponds to a subset of our parameter space. Not only does this observation provide the first tentative evidence of a volatile-rich secondary atmosphere on an ultra-short period planet, it shows that secondary atmospheres can be maintained for Gyr periods despite the potential for ongoing escape processes. However, understanding compositional fractionation in the escape of H-rich atmospheres is likely key to resolving the link between a planet's magma ocean stage and its current conditions (Wordsworth & Kreidberg, 2022).

HD 63433 d is a young Earth-sized exoplanet discovered in transit using TESS (Capistrant et al., 2024). Models and HST observations indicate that its outer neighbor (HD 63433 b) has lost its primordial H/He envelope (Zhang et al., 2022). If the more irradiated planet (HD 63433 d) has also lost its envelope then the composition of an overlying secondary atmosphere is likely to be significantly influenced by volcanism or volatile exchange with a permanent magma ocean. The equilibrium temperature of this planet ($\sim$1100 K) is larger than that of the most irradiated cases ($a = 1.054\text{AU} \Rightarrow T_{\text{eqm}} \sim 885\text{K}$, Figure 6) modeled in this study, which indicates that it may maintain a permanent magma ocean. HD 63433 d can potentially provide an analog for early Earth following the Moon-forming impact (Canup & Asphaug, 2001; Tonks & Melosh, 1993; Warren, 1985). The young age of this planet brings opportunities for direct inferences of planetary properties by comparison of observations with numerical models like PROTEUS. Future studies should consider the evolution and current state of this planet in greater detail.

With solidification comes outgassing of water (among other volatiles), shown in the bottom row of Figure 8 in which solidified cases have steamy atmospheres. Across solidified cases, the H_2O mole fraction varies smoothly with the oxygen fugacity and C/H ratio (bottom left panel) since atmospheric composition is no longer controlled by large amounts of melt. This behavior is also present at higher $[H]$, but only in the absence of any significant amount of silicate melt since the H_2O will otherwise favorably dissolve into the interior of the planet. This makes the mole fraction of H_2O a useful tracer for a recently solidified surface, despite not being the only driver behind the phase state. This will be less applicable as the planet continues to evolve and the hydrogen escapes to space.

Gases beyond H_2O contribute to the opacity of these atmospheres, thereby impacting their cooling times or relaxation to radiative equilibrium. However, even for a pure-steam case we find that the post-runaway transition occurs at higher temperatures when modeled with the most up-to-date linelists, in contrast to models using HITRAN-derived opacities. Future work should explore the impacts of additional sources of atmospheric opacity. For example, CO and H_2-H_2O collisional continua at high pressure and temperature (Karman et al., 2019).

It has been previously suggested that the mass, radii, and spectroscopic observations of sub-Neptune planets can be explained by the presence of magma oceans underneath thick H_2 dominated atmospheres (Shorttle et al., 2024). H_2 dominated atmospheres are common on permanent magma ocean planets arising from our grid, so it may be possible that these sub-Neptunes have maintained molten surfaces since their formation with energy loss limited by atmospheric blanketing and sufficient instellations, confirming previous models with simpler atmospheric approaches (Vazan et al., 2018). For example, Case 608 has a reducing mantle and large hydrogen inventory ($a = 1.054\text{AU}$, $fO_2 = \text{IW} - 5$, $C/H = 2$, $[H] = 10$) which allows it to reach global radiative equilibrium with an H_2-dominated atmosphere $\left(p_{H_2} = 1038\,\text{bar}\right)$ containing significant amounts of CO (329 bar) and CH_4 (103 bar). It is likely that such an atmosphere—particularly one buffered by volatiles dissolved in the mantle—could resist escape if formed around a sufficiently massive interior (Misener & Schlichting, 2021). In such a case, the redox evolution of the interior would dictate the post-H-escape composition of its secondary atmosphere (Lichtenberg, 2021; Lichtenberg & Miguel, 2024).

It is unreasonable to assume that all planets (both within and external to the Solar System) have a similar or Earth-like mineralogy, redox state, and volatile endowment (Gaillard et al., 2021; Guimond et al., 2023; Lichtenberg & Miguel, 2024; Putirka & Xu, 2021). Our simulations show that—at a fixed planet mass, instellation, and radius—the evolution of a magma ocean planet is strongly dependent on the properties of its semi-molten interior (Meier et al., 2023). This is directly reflected in the composition of the overlying atmosphere, both before and after the

magma ocean solidifies (if it does, depending also on the properties of the mantle). It is therefore also unreasonable to assume that a given planet (mass, instellation, etc.) will be solidified or molten without intimate knowledge of these other parameters. However, polluted white dwarfs provide an opportunity to probe the mineralogy and elemental compositions of exoplanets and can therefore provide insight into which evolutionary pathways are compatible with contemporary observations of exoplanets (Doyle, Klein, et al., 2019; Doyle, Young, et al., 2019; Xu & Bonsor, 2021). Observations of multiple exoplanets orbiting the same host star may also be helpful in lifting this degeneracy, since they will have closely related compositions but different instellations; characterizing their present states and comparing with evolutionary models (such as PROTEUS) may thereby constrain their interior properties. Similarly, these generalized planetary evolution models can also be applied to planets within the solar system, where direct and in-situ measurements may provide further constraints on the physics (Gillmann et al., 2024; Salvador et al., 2023).

The results presented in Section 3.6 indicate that these atmospheres on lava worlds may present radiative layers despite our assumption that they are fully convective below the stratosphere. This follows from the predictions of Selsis et al. (2023). However, it is also shown that some planets which maintain permanent magma oceans (e.g., Case 205 - Figure 10) are still able to remain convectively unstable in near-surface layers. Case 714, which outgasses a large steam atmosphere while solidifying, becomes weakly stable to convection near the surface under the thick steam atmosphere outgassed from the magma ocean. Calculation of an energy-conserving atmospheric temperature structure (and resultant energy fluxes) would also provide more accurate values for energy loss to space, potentially changing the solidification times calculated in this work (Salvador et al., 2017). Although JANUS prescribes a temperature profile for the atmosphere in a similar manner to previous works (Hamano et al., 2015; Lebrun et al., 2013; Lichtenberg et al., 2021; Nikolaou et al., 2019), it is possible that cases in our grid which do not solidify would do so in reality. Whether these atmospheres generally stay convective is seemingly not trivial to answer, so further investigation using a more comprehensive atmosphere model is merited. This should be explored for a range of atmospheric compositions generated from interior outgassing, ideally with the inclusion of compositional criteria for convective inhibition (Innes et al., 2023).

4.2. Limitations

Our simulations show that cases at $a \leq 0.527$ AU are completely dry at termination due to the combinations of high surface temperatures and comparatively low surface pressures from volatile dissolution. This means that volatile condensation does not occur, which precludes cloud formation but leaves open the possibility of photochemical haze production (Bergin et al., 2023; Maillard et al., 2023). Similarly, Lebrun et al. (2013) found that rainout is unlikely to occur at $a < 0.66$ AU for planets orbiting the Sun. Shallow regions of moist H_2O convection occur for a subset of cases at 0.737 AU. At $a \geq 1.054$ AU, moist convection and/or equilibrium saturation occurs in the upper atmosphere for almost all cases. This corresponds to solidified planets (panel k of Figure 5) where the mole fraction H_2O of water is large. Optically thick water clouds would reflect stellar radiation and absorb upwelling radiation, so it is unclear whether they would prolong or foreshorten magma ocean solidification (R. T. Pierrehumbert, 2010; Salvador et al., 2017). Rainout of H_2O could allow sufficient infrared transmission such that these planets escape the runaway greenhouse regime after some time. Future work should explore the role of aerosols in magma ocean evolution.

Atmospheric escape would act to remove volatiles from the system. However, due to the prescriptive nature of our atmosphere model, calculations of escape rate would offer little investigative value and are thus neglected. The equilibrium chemistry calculated for Case 714 (Figure 9) yields only minor abundances of low molecular weight species (H_2, CO), so it is possible that this atmosphere would be maintained against significant escape for the duration of this simulation. However, more complete calculations of the chemistry would be required to determine the speciation of elements in the regions of the upper atmosphere from which escape is occurring (Nicholls et al., 2023; Tsai et al., 2021). Together, chemistry and escape could influence outgassing rates—subject to sufficient mixing—through transport of volatiles from the surface into the aloft regions, which is then compensated by further outgassing (Wordsworth et al., 2018). Chemistry and escape can also act to distil the planet's total volatile content through the loss of low molecular weight species, thereby reducing the opacity and increasing radiative emission to space (Cherubim et al., 2024; Wordsworth et al., 2018). Together, chemistry and escape are expected to shorten magma ocean lifetimes compared to the calculations made in this work. Uncertainties in volatile accretion, however, could partially compensate for these processes (Lichtenberg & Clement, 2022; Venturini et al., 2020; Zahnle et al., 2020). Future work should consider simulating escape

processes self-consistently with magma ocean evolution, particularly in the context of highly irradiated rocky planets around M-type stars such as TRAPPIST-1b (Zieba et al., 2023).

We do not include tidal effects on the interior which could be significant source of heating for planets within tightly packed systems or on elliptical orbits (Bolmont et al., 2013; Bower et al., 2019; Hay & Matsuyama, 2019; Seligman et al., 2024). Our interior model, which is able to resolve melt-crystal separation as the magma ocean evolves, shows that interior energy transport by convection is largely offset by other transport processes. In the case of tidal heating dissipated near the surface, this could act to extend magma ocean lifetimes and potentially expose a greater fraction of a planet's volatile inventory to escape.

In this work we use a mass-balance approach to simultaneously solve for chemical and dissolution equilibrium, but only for a small set of volatiles. Rock vapors (e.g., SiO) are expected to be present in the atmospheres of magma ocean planets to various degrees (Wolf et al., 2023), potentially impacting their radiation environment and inducing upper-atmosphere thermal inversions (Piette et al., 2023; Zilinskas et al., 2023). The latter two works solve for chemical and dissolution equilibrium as separate processes, obtaining the total gas budgets by adding the results of each calculation. Falco et al. (2024) self-consistently solved for chemical and dissolution equilibrium of rock vapors and volatiles, finding that it is necessary to solve for the whole system simultaneously. Both Falco et al. (2024) and Zilinskas et al. (2023) found that only small hydrogen budgets are required to prevent the formation of a thermal inversion in the atmosphere, since increased amounts of hydrogen promotes the abundance of H_2O and resultant infrared absorption. The transition between inverted and non-inverted temperature profiles is narrow. Using the empirical fit for the transition derived by Falco et al. (2024) we find that all cases explored in our grid fall deep within the non-inverted regime. It is therefore expected that the inclusion of rock vapors would have only a minor impact on our results.

Finally, our simulations do not account for other erosion or delivery processes, such as those from giant impacts, which in the Solar System are though to have contributed to shaping the final volatile budget of the terrestrial planets (Schlichting & Mukhopadhyay, 2018). However, estimates of volatile losses by impact erosion differ by many orders of magnitude (Denman et al., 2022; Kegerreis et al., 2020; Lock & Stewart, 2024) and it is further unclear if late-accreting planetesimals would instead be a source of volatiles themselves (Lichtenberg & Clement, 2022). Hence, in this work we choose to restrict the volatile content to be fixed at the onset of our simulations, but future work shall consider a time-varying volatile accretion history during early thermal planetary evolution.

5. Conclusions

We have developed a coupled numerical model to simulate the rapid cooling stage of molten planets at arbitrary oxidation state, resulting in cases which either fully solidify or reach global radiative equilibrium while maintaining some amount of melt. Our conclusions are as follows.

1. The atmospheres which overlie magma oceans can have diverse compositions ranging from H_2- to CO_2-dominated, while recently solidified planets typically have atmospheres composed of H_2 and/or H_2O (by mole fraction).
2. Thermal blanketing by radiatively opaque atmospheres means that magma oceans spend most of their lifetime in a semi-molten state, with significant energy transport generated by crystallization and gravitational settling. Collisional absorption by H_2 is key to moderating magma ocean cooling, extending their lifetimes by 10–100s of Myr, even around Sun-like stars.
3. Whether or not a magma ocean solidifies depends not only on its instellation, but also on other properties such as the bulk C/H ratio, mantle oxygen fugacity, and bulk hydrogen inventory. It is thus critically important to consider a wide range of initial conditions when using observations of a planet to constrain its historical evolution.
4. Radiative heating rates within these model atmospheres indicate that they maintain strong atmospheric convection while very hot and molten. However, it is possible that this convection shuts down at the surface at later points in their evolution. Future work should explore this in detail.

Our numerical framework enables future modeling to incorporate a range of additional physics self-consistently, such as: radiative-convective energy balance and chemical kinetics in the atmosphere, escape processes, tidal heating, stellar evolution, impacts and volatile delivery, and geochemical cycling. Inclusion of a number of these

properties will enable more complete exploration of the geophysical history of exoplanets in diverse environments. These avenues will be explored in future work. We particularly emphasize the importance of realistic atmospheric temperature structures and real-gas radiative transfer.

Data Availability Statement

The source code for PROTEUS (Nicholls (2024c)—Zenodo: https://doi.org/10.5281/zenodo.12190523, https://github.com/FormingWorlds/PROTEUS) and JANUS (Nicholls (2024a)—Zenodo: https://doi.org/10.5281/zenodo.12190459, https://github.com/FormingWorlds/JANUS) are available under the Apache 2.0 license. The source code for SPIDER (Bower et al., 2022) is available on GitHub (https://github.com/djbower/spider) under the GPL 3.0 license. The source code for SOCRATES with additional tools for handling opacities (Nicholls (2024d)—Zenodo: https://doi.org/10.5281/zenodo.12190852, https://github.com/nichollsh/SOCRATES) is available under the BSD 3-clause license. MORS (Johnstone et al., 2021) is available on GitHub (https://github.com/FormingWorlds/MORS) under the MIT license. Opacity data (Grimm et al., 2021) are available online on the University of Geneva DACE website.

Case-by-case data and plots, additional analysis software, and the figures used in this article are available under the Apache 2.0 license via the Open Science Framework (Nicholls (2024b)—https://doi.org/10.17605/OSF.IO/4EQHN).

Analysis was performed with Python, Numpy (Harris et al., 2020), Scipy (Virtanen et al., 2020), and Matplotlib (Hunter, 2007). Data were represented using the Scientific Color Maps (Crameri, 2023).

Acknowledgments
We thank our two anonymous reviewers for their valuable feedback which significantly improved this paper. H.N. was supported by the Clarendon Fund and the MT Scholarship Trust. T.L. was supported by the Branco Weiss Foundation, the Alfred P. Sloan Foundation (AEThER project, G202114194), and NASA's Nexus for Exoplanet System Science research coordination network (Alien Earths project, 80NSSC21K0593). R.T.P acknowledges support from the UK STFC and the AEThER project.

References

Abe, Y. (1993). Physical state of the very early Earth. *Lithos*, *30*(3), 223–235. https://doi.org/10.1016/0024-4937(93)90037-D

Abel, M., Frommhold, L., Li, X., & Hunt, K. L. C. (2011). Collision-induced absorption by H_2 pairs: From hundreds to thousands of Kelvin. *The Journal of Physical Chemistry A*, *115*(25), 6805–6812. https://doi.org/10.1021/jp109441f

Amundsen, D., Baraffe, I., Tremblin, P., Manners, J., Hayek, W., Mayne, N., & Acreman, D. (2014). Accuracy tests of radiation schemes used in hot Jupiter global circulation models. *Astronomy & Astrophysics*, *564*, A59. https://doi.org/10.1051/0004-6361/201323169

Amundsen, D. S., Tremblin, P., Manners, J., Baraffe, I., & Mayne, N. J. (2017). Treatment of overlapping gaseous absorption with the correlated-k method in hot Jupiter and brown dwarf atmosphere models. *A&*, *598*, A97. https://doi.org/10.1051/0004-6361/201629322

Andrault, D., Bolfan-Casanova, N., Nigro, G. L., Bouhifd, M. A., Garbarino, G., & Mezouar, M. (2011). Solidus and liquidus profiles of chondritic mantle: Implication for melting of the Earth across its history. *Earth and Planetary Science Letters*, *304*(1–2), 251–259. https://doi.org/10.1016/j.epsl.2011.02.006

Ardia, P., Hirschmann, M. M., Withers, A. C., & Stanley, B. D. (2013). Solubility of CH_4 in a synthetic basaltic melt, with applications to atmosphere–magma ocean–core partitioning of volatiles and to the evolution of the Martian atmosphere. *Geochimica et Cosmochimica Acta*, *114*, 52–71. https://doi.org/10.1016/j.gca.2013.03.028

Armstrong, L. S., Hirschmann, M. M., Stanley, B. D., Falksen, E. G., & Jacobsen, S. D. (2015). Speciation and solubility of reduced C–O–H–N volatiles in mafic melt: Implications for volcanism, atmospheric evolution, and deep volatile cycles in the terrestrial planets. *Geochimica et Cosmochimica Acta*, *171*, 283–302. https://doi.org/10.1016/j.gca.2015.07.007

Aufaristama, M., Hoskuldsson, A., Jonsdottir, I., Ulfarsson, M. O., & Thordarson, T. (2018). New insights for detecting and deriving thermal properties of lava flow using infrared satellite during 2014–2015 effusive eruption at Holuhraun, Iceland. *Remote Sensing*, *10*(1), 151. https://doi.org/10.3390/rs10010151

Balkan, E., Erkan, K., & Şalk, M. (2017). Thermal conductivity of major rock types in western and central Anatolia regions, Turkey. *Journal of Geophysics and Engineering*, *14*(4), 909–919. https://doi.org/10.1088/1742-2140/aa5831

Baraffe, I., Homeier, D., Allard, F., & Chabrier, G. (2015). New evolutionary models for pre-main sequence and main sequence low-mass stars down to the hydrogen-burning limit. *Astronomy & Astrophysics*, *577*, A42. https://doi.org/10.1051/0004-6361/201425481

Barklem, P., & Collet, R. (2016). Partition functions and equilibrium constants for diatomic molecules and atoms of astrophysical interest. *Astronomy & Astrophysics*, *588*, A96. https://doi.org/10.1051/0004-6361/201526961

Barth, P., Carone, L., Barnes, R., Noack, L., Mollière, P., & Henning, T. (2021). Magma ocean evolution of the TRAPPIST-1 planets. *Astrobiology*, *21*(11), 1325–1349. https://doi.org/10.1089/ast.2020.2277

Bergin, E. A., Kempton, E. M.-R., Hirschmann, M., Bastelberger, S. T., Teal, D. J., Blake, G. A., et al. (2023). Exoplanet volatile carbon content as a natural pathway for haze formation. *The Astrophysical Journal Letters*, *949*(1), L17. https://doi.org/10.3847/2041-8213/acd377

Bolmont, E., Selsis, F., Raymond, S. N., Leconte, J., Hersant, F., Maurin, A.-S., & Pericaud, J. (2013). Tidal dissipation and eccentricity pumping: Implications for the depth of the secondary eclipse of 55 Cancri e. *Astronomy & Astrophysics*, *556*, A17. https://doi.org/10.1051/0004-6361/201220837

Bonati, I., Lichtenberg, T., Bower, D. J., Timpe, M. L., & Quanz, S. P. (2019). Direct imaging of molten protoplanets in nearby young stellar associations. *Astronomy & Astrophysics*, *621*, A125. https://doi.org/10.1051/0004-6361/201833158

Borg, L. E., Shearer, C. K., Asmerom, Y., & Papike, J. J. (2004). Prolonged KREEP magmatism on the Moon indicated by the youngest dated lunar igneous rock. *Nature*, *432*(7014), 209–211. https://doi.org/10.1038/nature03070

Borysow, A., & Frommhold, L. (1991). Pressure-induced absorption in the infrared: A data base for the modelling of planetary atmospheres. *Journal of Geophysical Research*, *96*(E2), 17501–17506. https://doi.org/10.1029/91JE01683

Boukrouche, R., Lichtenberg, T., & Pierrehumbert, R. T. (2021). Beyond runaway: Initiation of the post-runaway greenhouse state on rocky exoplanets. *The Astrophysical Journal*, *919*(2), 130. https://doi.org/10.3847/1538-4357/ac1345

Bower, D. J., Hakim, K., Sossi, P. A., & Sanan, P. (2022). Retention of water in terrestrial magma oceans and carbon-rich early atmospheres. *The Planetary Science Journal*, *3*(4), 93. https://doi.org/10.3847/PSJ/ac5fb1

Bower, D. J., Kitzmann, D., Wolf, A. S., Sanan, P., Dorn, C., & Oza, A. V. (2019). Linking the evolution of terrestrial interiors and an early outgassed atmosphere to astrophysical observations. *Astronomy & Astrophysics*, *631*, A103. https://doi.org/10.1051/0004-6361/201935710

Bower, D. J., Sanan, P., & Wolf, A. S. (2018). Numerical solution of a non-linear conservation law applicable to the interior dynamics of partially molten planets. *Physics of the Earth and Planetary Interiors*, *274*, 49–62. https://doi.org/10.1016/j.pepi.2017.11.004

Broadley, M. W., Bekaert, D. V., Piani, L., Füri, E., & Marty, B. (2022). Origin of life-forming volatile elements in the inner solar system. *Nature*, *611*(7935), 245–255. https://doi.org/10.1038/s41586-022-05276-x

Canup, R. M., & Asphaug, E. (2001). Origin of the Moon in a giant impact near the end of the Earth's formation. *Nature*, *412*(6848), 708–712. https://doi.org/10.1038/35089010

Capistrant, B. K., Soares-Furtado, M., Vanderburg, A., Jankowski, A., Mann, A. W., Ross, G., et al. (2024). TESS Hunt for Young and Maturing Exoplanets (THYME). XI. An Earth-sized Planet Orbiting a Nearby, Solar-like Host in the 400 myr Ursa Major Moving Group. *The Astronomical Journal*, *167*(2), 54. https://doi.org/10.3847/1538-3881/ad1039

Cartier, C., & Wood, B. J. (2019). The role of reducing conditions in building Mercury. *Elements*, *15*(1), 39–45. https://doi.org/10.2138/gselements.15.1.39

Chao, K.-H., deGraffenried, R., Lach, M., Nelson, W., Truax, K., & Gaidos, E. (2021). Lava worlds: From early earth to exoplanets. *Chemie der Erde/Geochemistry*, *81*(2), 125735. https://doi.org/10.1016/j.chemer.2020.125735

Chase, M. (1998). *NIST-JANAF thermochemical tables* (4th ed.). American Institute of Physics.

Chen, G., Laane, J., Wheeler, S. E., & Zhang, Z. (2011). Greenhouse gas molecules: A mathematical perspective. *Notices of the AMS*, *58*(10), 1421–1434.

Cherubim, C., Wordsworth, R., Hu, R., & Shkolnik, E. (2024). Strong fractionation of deuterium and helium in sub-Neptune atmospheres along the Radius Valley. *The Astrophysical Journal*, *967*(2), 139. https://doi.org/10.3847/1538-4357/ad3e77

Chibati, N., Géraud, Y., & Essa, K. S. (2022). Petrophysical characterization and thermal conductivity prediction of serpentinized peridotites. *Geophysical Journal International*, *231*(3), 1786–1805. https://doi.org/10.1093/gji/ggac288

Crameri, F. (2023). Scientific colour maps. *Zenodo*. https://doi.org/10.5281/zenodo.8409685

Cronin, T. W. (2014). On the choice of average solar zenith angle. *Journal of the Atmospheric Sciences*, *71*(8), 2994–3003. https://doi.org/10.1175/JAS-D-13-0392.1

Denman, T. R., Leinhardt, Z. M., & Carter, P. J. (2022). Atmosphere loss in oblique Super-Earth collisions. *Monthly Notices of the Royal Astronomical Society*, *513*(2), 1680–1700. https://doi.org/10.1093/mnras/stac923

Dixon, J. E., & Pan, V. (1995). Determination of the molar absorptivity of dissolved carbonate in Basanitic glass. *American Mineralogist*, *80*(11–12), 1339–1342. https://doi.org/10.2138/am-1995-11-1224

Dorn, C., & Lichtenberg, T. (2021). Hidden water in magma ocean exoplanets. *The Astrophysical Journal*, *922*(1), L4. https://doi.org/10.3847/2041-8213/ac33af

Doyle, A. E., Klein, B., Zuckerman, B., Schlichting, H. E., & Young, E. D. (2019). Exoplanetary oxygen fugacities from polluted white dwarf stars. *Proceedings of the International Astronomical Union*, *15*(S357), 28–32. https://doi.org/10.1017/S1743921320000939

Doyle, A. E., Young, E. D., Klein, B., Zuckerman, B., & Schlichting, H. E. (2019). Oxygen fugacities of extrasolar rocks: Evidence for an Earth-like geochemistry of exoplanets. *Science*, *366*(6463), 356–359. https://doi.org/10.1126/science.aax3901

Drażkowska, J., Bitsch, B., Lambrechts, M., Mulders, G. D., Harsono, D., Vazan, A., et al. (2023). Planet Formation theory in the era of ALMA and Kepler: From Pebbles to exoplanets. In S. Inutsuka, Y. Aikawa, T. Muto, K. Tomida, & M. Tamura (Eds.), *Protostars and planets vii* (Vol. 534, p. 717). https://doi.org/10.48550/arXiv.2203.09759

Dudhia, A. (2017). The reference forward model (RFM). *Journal of Quantitative Spectroscopy and Radiative Transfer*, *186*, 243–253. (Satellite Remote Sensing and Spectroscopy: Joint ACE-Odin Meeting, October 2015). https://doi.org/10.1016/j.jqsrt.2016.06.018

Edwards, J. M., & Slingo, A. (1996). Studies with a flexible new radiation code. I: Choosing a configuration for a large-scale model. *Quarterly Journal of the Royal Meteorological Society*, *122*(531), 689–719. https://doi.org/10.1002/qj.49712253107

Elkins-Tanton, L. (2008). Linked magma ocean solidification and atmospheric growth for Earth and Mars. *Earth and Planetary Science Letters*, *271*(1), 181–191. https://doi.org/10.1016/j.epsl.2008.03.062

Elkins-Tanton, L. (2012). Magma oceans in the inner solar system. *Annual Review of Earth and Planetary Sciences*, *40*(1), 113–139. https://doi.org/10.1146/annurev-earth-042711-105503

Essack, Z., Seager, S., & Pajusalu, M. (2020). Low-albedo surfaces of lava worlds. *The Astrophysical Journal*, *898*(2), 160. https://doi.org/10.3847/1538-4357/ab9cba

Falco, A., Tremblin, P., Charnoz, S., Ridgway, R. J., & Lagage, P.-O. (2024). Hydrogenated atmospheres of lava planets: Atmospheric structure and emission spectra. *Astronomy & Astrophysics*, *683*, A194. https://doi.org/10.1051/0004-6361/202347650

Gaillard, F., Bouhifd, M. A., Füri, E., Malavergne, V., Marrocchi, Y., Noack, L., et al. (2021). The diverse planetary ingassing/outgassing paths produced over billions of years of magmatic activity. *Space Science Reviews*, *217*(1), 22. https://doi.org/10.1007/s11214-021-00802-1

Gallet, F., & Bouvier, J. (2013). Improved angular momentum evolution model for solar-like stars. *Astronomy & Astrophysics*, *556*, A36. https://doi.org/10.1051/0004-6361/201321302

Gillmann, C., Chassefière, E., & Lognonné, P. (2009). A consistent picture of early hydrodynamic escape of Venus atmosphere explaining present Ne and Ar isotopic ratios and low oxygen atmospheric content. *Earth and Planetary Science Letters*, *286*(3–4), 503–513. https://doi.org/10.1016/j.epsl.2009.07.016

Gillmann, C., Hakim, K., Lourenço, D., Quanz, S. P., & Sossi, P. A. (2024). Interior controls on the habitability of rocky planets. *Space: Science and Technology*, *4*, 0075. https://doi.org/10.34133/space.0075

Goldblatt, C., Robinson, T. D., Zahnle, K. J., & Crisp, D. (2013). Low simulated radiation limit for runaway greenhouse climates. *Nature Geoscience*, *6*(8), 661–667. https://doi.org/10.1038/ngeo1892

Goody, R. M., & Yung, Y. L. (1989). *Atmospheric radiation: Theoretical basis. Cary*. Oxford University Press.

Gordon, I. E., Rothman, L. S., Hargreaves, R. J., Hashemi, R., Karlovets, E. V., Skinner, F. M., et al. (2022). The HITRAN2020 molecular spectroscopic database. *Journal of Quantitative Spectroscopy and Radiative Transfer*, *277*, 107949. https://doi.org/10.1016/j.jqsrt.2021.107949

Graham, R. J., Lichtenberg, T., Boukrouche, R., & Pierrehumbert, R. T. (2021). A multispecies pseudoadiabat for simulating condensable-rich exoplanet atmospheres. *The Planetary Science Journal*, *2*(5), 207. https://doi.org/10.3847/PSJ/ac214c

Grimm, S. L., Malik, M., Kitzmann, D., Guzmán-Mesa, A., Hoeijmakers, H. J., Fisher, C., et al. (2021). HELIOS-K 2.0 opacity calculator and open-source opacity database for exoplanetary atmospheres. *The Astrophysical Journal - Supplement Series*, *253*(1), 30. https://doi.org/10.3847/1538-4365/abd773

Gu, J. T., Peng, B., Ji, X., Zhang, J., Yang, H., Hoyos, S., et al. (2024). Composition of Earth's initial atmosphere and fate of accreted volatiles set by core formation and magma ocean redox evolution. *Earth and Planetary Science Letters*, *629*, 118618. https://doi.org/10.1016/j.epsl.2024.118618

Gueymard, C. A. (2004). The Sun's total and spectral irradiance for solar energy applications and solar radiation models. *Solar Energy*, *76*(4), 423–453. https://doi.org/10.1016/j.solener.2003.08.039

Guillot, T. (2010). On the radiative equilibrium of irradiated planetary atmospheres. *Astronomy & Astrophysics*, *520*, A27. https://doi.org/10.1051/0004-6361/200913396

Guimond, C. M., Shorttle, O., Jordan, S., & Rudge, J. F. (2023). A mineralogical reason why all exoplanets cannot be equally oxidizing. *Monthly Notices of the Royal Astronomical Society*, *525*(3), 3703–3717. https://doi.org/10.1093/mnras/stad2486

Hamano, K., Abe, Y., & Genda, H. (2013). Emergence of two types of terrestrial planet on solidification of magma ocean. *Nature*, *497*(7451), 607–610. https://doi.org/10.1038/nature12163

Hamano, K., Kawahara, H., Abe, Y., Onishi, M., & Hashimoto, G. L. (2015). Lifetime and spectral evolution of a magma ocean with a steam atmosphere: Its detectability by future direct imaging. *The Astrophysical Journal*, *806*(2), 216. https://doi.org/10.1088/0004-637X/806/2/216

Hamilton, D. L., Burnham, C. W., & Osborn, E. F. (1964). The solubility of water and effects of oxygen fugacity and water content on crystallization in mafic magmas. *Journal of Petrology*, *5*(1), 21–39. https://doi.org/10.1093/petrology/5.1.21

Harris, C. R., Millman, K. J., van der Walt, S. J., Gommers, R., Virtanen, P., Cournapeau, D., et al. (2020). Array programming with NumPy. *Nature*, *585*(7825), 357–362. https://doi.org/10.1038/s41586-020-2649-2

Hay, H. C. F. C., & Matsuyama, I. (2019). Tides between the TRAPPIST-1 planets. *The Astrophysical Journal*, *875*(1), 22. https://doi.org/10.3847/1538-4357/ab0c21

Hedges, C., Hughes, A., Zhou, G., David, T. J., Becker, J., Giacalone, S., et al. (2021). TOI-2076 and TOI-1807: Two young, comoving planetary systems within 50 pc identified by TESS that are ideal candidates for further follow up. *The Astronomical Journal*, *162*(2), 54. https://doi.org/10.3847/1538-3881/ac06cd

Hier-Majumder, S., & Hirschmann, M. M. (2017). The origin of volatiles in the Earth's mantle. *Geochemistry, Geophysics, Geosystems*, *18*(8), 3078–3092. https://doi.org/10.1002/2017GC006937

Hu, R., Bello-Arufe, A., Zhang, M., Paragas, K., Zilinskas, M., van Buchem, C., et al. (2024). A secondary atmosphere on the rocky exoplanet 55 Cancri e. *arXiv e-prints, arXiv:2405.04744*, *630*(8017), 609–612. https://doi.org/10.48550/arXiv.2405.04744

Hunter, J. D. (2007). Matplotlib: A 2d graphics environment. *Computing in Science & Engineering*, *9*(3), 90–95. https://doi.org/10.1109/MCSE.2007.55

Ikoma, M., Elkins-Tanton, L., Hamano, K., & Suckale, J. (2018). Water partitioning in planetary embryos and protoplanets with Magma Oceans. *Space Science Reviews*, *214*(4), 76. https://doi.org/10.1007/s11214-018-0508-3

Innes, H., Tsai, S.-M., & Pierrehumbert, R. T. (2023). The runaway greenhouse effect on hycean worlds. *The Astrophysical Journal*, *953*(2), 168. https://doi.org/10.3847/1538-4357/ace346

Johnstone, C. P. (2017). On the fast magnetic rotator regime of stellar winds. *Astronomy & Astrophysics*, *598*, A24. https://doi.org/10.1051/0004-6361/201629609

Johnstone, C. P., Bartel, M., & Güdel, M. (2021). The active lives of stars: A complete description of the rotation and XUV evolution of F, G, K, and M dwarfs. *Astronomy & Astrophysics*, *649*, A96. https://doi.org/10.1051/0004-6361/202038407

Karman, T., Gordon, I. E., van der Avoird, A., Baranov, Y. I., Boulet, C., Drouin, B. J., et al. (2019). Update of the HITRAN collision-induced absorption section. *Icarus*, *328*, 160–175. https://doi.org/10.1016/j.icarus.2019.02.034

Kasting, J. F., Whitmire, D. P., & Reynolds, R. T. (1993). Habitable zones around main sequence stars. *Icarus*, *101*(1), 108–128. https://doi.org/10.1006/icar.1993.1010

Katyal, N., Nikolaou, A., Godolt, M., Grenfell, J. L., Tosi, N., Schreier, F., & Rauer, H. (2019). Evolution and spectral response of a steam atmosphere for early earth with a coupled climate-interior model. *The Astrophysical Journal*, *875*(1), 31. https://doi.org/10.3847/1538-4357/ab0d85

Kegerreis, J. A., Eke, V. R., Catling, D. C., Massey, R. J., Teodoro, L. F. A., & Zahnle, K. J. (2020). Atmospheric erosion by giant impacts onto terrestrial planets: A scaling law for any speed, angle, mass, and density. *The Astrophysical Journal*, *901*(2), L31. https://doi.org/10.3847/2041-8213/abb5fb

Khan, A., Huang, D., Durán, C., Sossi, P. A., Giardini, D., & Murakami, M. (2023). Evidence for a liquid silicate layer atop the martian core. *Nature*, *622*(7984), 718–723. https://doi.org/10.1038/s41586-023-06586-4

Kimura, T., & Ikoma, M. (2020). Formation of aqua planets with water of nebular origin: Effects of water enrichment on the structure and mass of captured atmospheres of terrestrial planets. *Monthly Notices of the Royal Astronomical Society*, *496*(3), 3755–3766. https://doi.org/10.1093/mnras/staa1778

Komabayasi, M. (1967). Discrete equilibrium temperatures of a hypothetical planet with the atmosphere and the hydrosphere of one component-two phase system under constant solar radiation. *Journal of the Meteorological Society of Japan. Ser. II*, *45*(1), 137–139. https://doi.org/10.2151/jmsj1965.45.1_137

Kopparapu, R. K., Ramirez, R., Kasting, J. F., Eymet, V., Robinson, T. D., Mahadevan, S., et al. (2013). Habitable zones around main-sequence stars: New estimates. *The Astrophysical Journal*, *765*(2), 131. https://doi.org/10.1088/0004-637X/765/2/131

Korotev, R. L., & Gillis, J. J. (2001). A new look at the Apollo 11 regolith and KREEP. *Journal of Geophysical Research*, *106*(E6), 12339–12353. https://doi.org/10.1029/2000JE001336

Krijt, S., Kama, M., McClure, M., Teske, J., Bergin, E. A., Shorttle, O., et al. (2023). Chemical habitability: Supply and retention of life's essential elements during planet formation. In S. Inutsuka, Y. Aikawa, T. Muto, K. Tomida, & M. Tamura (Eds.), *Protostars and planets vii* (Vol. 534, p. 1031).

Krissansen-Totton, J. (2023). Implications of atmospheric nondetections for Trappist-1 inner planets on atmospheric retention prospects for outer planets. *The Astrophysical Journal Letters*, *951*(2), L39. https://doi.org/10.3847/2041-8213/acdc26

Krissansen-Totton, J., Fortney, J. J., Nimmo, F., & Wogan, N. (2021). Oxygen false positives on habitable zone planets around sun-like stars. *AGU Advances*, *2*(2), e00294. https://doi.org/10.1029/2020AV000294

Lacis, A. A., & Oinas, V. (1991). A description of the correlatedkdistribution method for modeling nongray gaseous absorption, thermal emission, and multiple scattering in vertically inhomogeneous atmospheres. *Journal of Geophysical Research*, *96*(D5), 9027–9063. https://doi.org/10.1029/90jd01945

Lammer, H., Leitzinger, M., Scherf, M., Odert, P., Burger, C., Kubyshkina, D., et al. (2020). Constraining the early evolution of Venus and Earth through atmospheric Ar, Ne isotope and bulk K/U ratios. *Icarus*, *339*, 113551. https://doi.org/10.1016/j.icarus.2019.113551

Lebrun, T., Massol, H., Chassefière, E., Davaille, A., Marcq, E., Sarda, P., et al. (2013). Thermal evolution of an early magma ocean in interaction with the atmosphere. *Journal of Geophysical Research: Planets*, *118*(6), 1155–1176. https://doi.org/10.1002/jgre.20068

Li, G., Gordon, I. E., Rothman, L. S., Tan, Y., Hu, S.-M., Kassi, S., et al. (2015). Rovibrational line lists for nine isotopologues of the CO molecule in the X1Σ+ ground electronic state. *The Astrophysical Journal - Supplement Series*, *216*(1), 15. https://doi.org/10.1088/0067-0049/216/1/15

Libourel, G., Marty, B., & Humbert, F. (2003). Nitrogen solubility in basaltic melt. Part I. Effect of oxygen fugacity. *Geochimica et Cosmochimica Acta*, *67*(21), 4123–4135. https://doi.org/10.1016/S0016-7037(03)00259-X

Lichtenberg, T. (2021). Redox hysteresis of super-Earth exoplanets from magma ocean circulation. *The Astrophysical Journal*, *914*(1), L4. https://doi.org/10.3847/2041-8213/ac0146

Lichtenberg, T., Bower, D. J., Hammond, M., Boukrouche, R., Sanan, P., Tsai, S., & Pierrehumbert, R. T. (2021). Vertically resolved magma ocean–protoatmosphere evolution: H_2, H_2O, CO_2, CH_4, CO, O_2, and N_2 as primary absorbers. *Journal of Geophysical Research: Planets*, *126*(2). https://doi.org/10.1029/2020JE006711

Lichtenberg, T., & Clement, M. S. (2022). Reduced late bombardment on rocky exoplanets around M dwarfs. *The Astrophysical Journal Letters*, *938*(1), L3. https://doi.org/10.3847/2041-8213/ac9521

Lichtenberg, T., & Miguel, Y. (2024). Super-Earths and earth-like exoplanets. *arXiv e-prints, arXiv:2405.04057*. https://doi.org/10.48550/arXiv.2405.04057

Lichtenberg, T., Schaefer, L. K., Nakajima, M., & Fischer, R. A. (2023). Geophysical evolution during rocky planet formation. In S. Inutsuka, Y. Aikawa, T. Muto, K. Tomida, & M. Tamura (Eds.), *Protostars and planets vii* (Vol. 534, p. 907). https://doi.org/10.48550/arXiv.2203.10023

Lock, S. J., & Stewart, S. T. (2024). Atmospheric loss in giant impacts depends on preimpact surface conditions. *Planetary Science Journal*, *5*(2), 28. https://doi.org/10.3847/PSJ/ad0b16

Maillard, J., Carrasco, N., Rüger, C. P., Chatain, A., Schmitz-Afonso, I., Weisbrod, C. R., et al. (2023). Humid evolution of haze in the atmosphere of super-earths in the habitable zone. *Astrobiology*, *23*(6), 723–732. https://doi.org/10.1089/ast.2022.0021

Massol, H., Hamano, K., Tian, F., Ikoma, M., Abe, Y., Chassefière, E., et al. (2016). Formation and evolution of protoatmospheres. *Space Science Reviews*, *205*(1–4), 153–211. https://doi.org/10.1007/s11214-016-0280-1

Maurice, M., Dasgupta, R., & Hassanzadeh, P. (2024). Volatile atmospheres of lava worlds. *arXiv e-prints, arXiv:2405.09284*, *688*, A47. https://doi.org/10.48550/arXiv.2405.09284

McKenzie, D. (2011). Compaction and crystallization in magma chambers: Towards a model of the Skaergaard intrusion. *Journal of Petrology*, *52*(5), 905–930. https://doi.org/10.1093/petrology/egr009

Meier, T. G., Bower, D. J., Lichtenberg, T., Hammond, M., & Tackley, P. J. (2023). Interior dynamics of super-Earth 55 Cancri e. *Astronomy & Astrophysics*, *678*, A29. https://doi.org/10.1051/0004-6361/202346950

Misener, W., & Schlichting, H. E. (2021). To cool is to keep: Residual H/He atmospheres of super-earths and sub-neptunes. *Monthly Notices of the Royal Astronomical Society*, *503*(4), 5658–5674. https://doi.org/10.1093/mnras/stab895

Mlawer, E. J., Cady-Pereira, K. E., Mascio, J., & Gordon, I. E. (2023). The inclusion of the MT_CKD water vapor continuum model in the HITRAN molecular spectroscopic database. *Journal of Quantitative Spectroscopy and Radiative Transfer*, *306*, 108645. https://doi.org/10.1016/j.jqsrt.2023.108645

Mlawer, E. J., Payne, V. H., Moncet, J. L., Delamere, J. S., Alvarado, M. J., & Tobin, D. C. (2012). Development and recent evaluation of the MT_CKD model of continuum absorption. *Philosophical Transactions of the Royal Society of London,Series A*, *370*(1968), 2520–2556. https://doi.org/10.1098/rsta.2011.0295

Monteux, J., Andrault, D., & Samuel, H. (2016). On the cooling of a deep terrestrial magma ocean. *Earth and Planetary Science Letters*, *448*, 140–149. https://doi.org/10.1016/j.epsl.2016.05.010

Nakajima, M., Golabek, G. J., Wünnemann, K., Rubie, D. C., Burger, C., Melosh, H. J., et al. (2021). Scaling laws for the geometry of an impact-induced magma ocean. *Earth and Planetary Science Letters*, *568*, 116983. https://doi.org/10.1016/j.epsl.2021.116983

Neri, A. (1998). A local heat transfer analysis of lava cooling in the atmosphere: Application to thermal diffusion-dominated lava flows. *Journal of Volcanology and Geothermal Research*, *81*(3), 215–243. https://doi.org/10.1016/S0377-0273(98)00010-9

Nicholls, H. (2024a). Janus [Software]. *Zenodo*. https://doi.org/10.5281/zenodo.12190459

Nicholls, H. (2024b). Magma ocean proteus/janus grid exploration [Dataset]. https://doi.org/10.17605/OSF.IO/GXQFH

Nicholls, H. (2024c). Proteus [Software]. *Zenodo*. https://doi.org/10.5281/zenodo.12190523

Nicholls, H. (2024d). Socrates [Software]. *Zenodo*. https://doi.org/10.5281/zenodo.12190852

Nicholls, H., Hébrard, E., Venot, O., Drummond, B., & Evans, E. (2023). Temperature-chemistry coupling in the evolution of gas giant atmospheres driven by stellar flares. *Monthly Notices of the Royal Astronomical Society*, *523*(4), 5681–5702. https://doi.org/10.1093/mnras/stad1734

Nicklas, R. W., Puchtel, I. S., & Ash, R. D. (2018). Redox state of the Archean mantle: Evidence from V partitioning in 3.5–2.4 Ga komatiites. *Geochimica et Cosmochimica Acta*, *222*, 447–466. https://doi.org/10.1016/j.gca.2017.11.002

Nikolaou, A., Katyal, N., Tosi, N., Godolt, M., Grenfell, J. L., & Rauer, H. (2019). What factors affect the duration and outgassing of the terrestrial magma ocean? *The Astrophysical Journal*, *875*(1), 11. https://doi.org/10.3847/1538-4357/ab08ed

O'Neill, H. S., & Eggins, S. M. (2002). The effect of melt composition on trace element partitioning: An experimental investigation of the activity coefficients of FeO, NiO, CoO, MoO2 and MoO3 in silicate melts. *Chemical Geology*, *186*(1), 151–181. https://doi.org/10.1016/S0009-2541(01)00414-4

Ortenzi, G., Noack, L., Sohl, F., Guimond, C. M., Grenfell, J. L., Dorn, C., et al. (2020). Mantle redox state drives outgassing chemistry and atmospheric composition of rocky planets. *Scientific Reports*, *10*(1), 10907. https://doi.org/10.1038/s41598-020-67751-7

Pierrehumbert, R., & Gaidos, E. (2011). Hydrogen greenhouse planets beyond the habitable zone. *The Astrophysical Journal Letters*, *734*(1), L13. https://doi.org/10.1088/2041-8205/734/1/L13

Pierrehumbert, R. T. (2010). *Principles of planetary climate*. Cambridge University Press.

Piette, A. A. A., Gao, P., Brugman, K., Shahar, A., Lichtenberg, T., Miozzi, F., & Driscoll, P. (2023). Rocky planet or water world? Observability of low-density lava world atmospheres. *The Astrophysical Journal*, *954*(1), 29. https://doi.org/10.3847/1538-4357/acdef2

Polyansky, O. L., Kyuberis, A. A., Zobov, N. F., Tennyson, J., Yurchenko, S. N., & Lodi, L. (2018). ExoMol molecular line lists XXX: A complete high-accuracy line list for water. *Monthly Notices of the Royal Astronomical Society*, *480*(2), 2597–2608. https://doi.org/10.1093/mnras/sty1877

Putirka, K. D., & Xu, S. (2021). Polluted white dwarfs reveal exotic mantle rock types on exoplanets in our solar neighborhood. *Nature Communications*, *12*(1), 6168. https://doi.org/10.1038/s41467-021-26403-8

Ramirez, R. M., & Kaltenegger, L. (2017). A volcanic hydrogen habitable zone. *The Astrophysical Journal Letters*, *837*(1), L4. https://doi.org/10.3847/2041-8213/aa60c8

Robinson, T. D., & Catling, D. C. (2012). An analytic radiative–convective model for planetary atmospheres. *The Astrophysical Journal*, *757*(1), 104. https://doi.org/10.1088/0004-637X/757/1/104

Rollinson, H., Adetunji, J., Lenaz, D., & Szilas, K. (2017). Archaean chromitites show constant Fe3+/ΣFe in Earth's asthenospheric mantle since 3.8 Ga. *Lithos*, *282–283*, 316–325. https://doi.org/10.1016/j.lithos.2017.03.020

Roueff, E., Abgrall, H., Czachorowski, P., Pachucki, K., Puchalski, M., & Komasa, J. (2019). The full infrared spectrum of molecular hydrogen*. *Astronomy & Astrophysics*, *630*, A58. https://doi.org/10.1051/0004-6361/201936249

Ruedas, T. (2017). Radioactive heat production of six geologically important nuclides. *Geochemistry, Geophysics, Geosystems*, *18*(9), 3530–3541. https://doi.org/10.1002/2017GC006997

Salvador, A., Avice, G., Breuer, D., Gillmann, C., Lammer, H., Marcq, E., et al. (2023). Magma Ocean, water, and the early atmosphere of Venus. *Space Science Reviews*, *219*(7), 51. https://doi.org/10.1007/s11214-023-00995-7

Salvador, A., Massol, H., Davaille, A., Marcq, E., Sarda, P., & Chassefière, E. (2017). The relative influence of H_2O and CO_2 on the primitive surface conditions and evolution of rocky planets. *Journal of Geophysical Research (Planets)*, *122*(7), 1458–1486. https://doi.org/10.1002/2017JE005286

Schaefer, L., & Fegley, B. (2017). Redox states of initial atmospheres outgassed on rocky planets and planetesimals. *The Astrophysical Journal*, *843*(2), 120. https://doi.org/10.3847/1538-4357/aa784f

Schaefer, L., Wordsworth, R. D., Berta-Thompson, Z., & Sasselov, D. (2016). Predictions of the atmospheric composition of GJ 1132b. *The Astrophysical Journal*, *829*(2), 63. https://doi.org/10.3847/0004-637X/829/2/63

Schlecker, M., Apai, D., Lichtenberg, T., Bergsten, G., Salvador, A., & Hardegree-Ullman, K. K. (2024). Bioverse: The habitable zone inner edge discontinuity as an imprint of runaway greenhouse climates on exoplanet demographics. *Planetary Science Journal*, *5*(1), 3. https://doi.org/10.3847/PSJ/acf57f

Schlichting, H. E., & Mukhopadhyay, S. (2018). Atmosphere impact losses. *Space Science Reviews*, *214*(1), 34. https://doi.org/10.1007/s11214-018-0471-z

Seligman, D. Z., Feinstein, A. D., Lai, D., Welbanks, L., Taylor, A. G., Becker, J., et al. (2024). Potential melting of extrasolar planets by tidal dissipation. *The Astrophysical Journal*, *961*(1), 22. https://doi.org/10.3847/1538-4357/ad0b82

Selsis, F., Leconte, J., Turbet, M., Chaverot, G., & Bolmont, m. (2023). A cool runaway greenhouse without surface magma ocean. *Nature*, *620*(7973), 287–291. https://doi.org/10.1038/s41586-023-06258-3

Sergeev, D. E., Mayne, N. J., Bendall, T., Boutle, I. A., Brown, A., Kavčič, I., et al. (2023). Simulations of idealised 3D atmospheric flows on terrestrial planets using LFRic-atmosphere. *Geoscientific Model Development*, *16*(19), 5601–5626. https://doi.org/10.5194/gmd-16-5601-2023

Shemansky, D. E. (1969). N2 Vegard–Kaplan system in absorption. *The Journal of Chemical Physics*, *51*(2), 689–700. https://doi.org/10.1063/1.1672058

Shorttle, O., Jordan, S., Nicholls, H., Lichtenberg, T., & Bower, D. J. (2024). Distinguishing oceans of water from magma on mini-Neptune K2-18b. *The Astrophysical Journal Letters*, *962*(1), L8. https://doi.org/10.3847/2041-8213/ad206e

Siggia, E. D. (1994). High Rayleigh number convection. *Annual Review of Fluid Mechanics*, *26*(1), 137–168. https://doi.org/10.1146/annurev.fl.26.010194.001033

Solomatov, V. (2015). Magma Oceans and primordial mantle differentiation. In G. Schubert (Ed.), *Treatise on geophysics* (Vol. 9, pp. 91–119). https://doi.org/10.1016/B978-044452748-6.00141-3

Solomatov, V. S. (2000). Fluid dynamics of a terrestrial magma ocean. In R. M. Canup & K. Righter (Eds.), *Origin of the Earth and Moon* (pp. 323–338). University of Arizona Press.

Solomatov, V. S., & Stevenson, D. J. (1993a). Nonfractional crystallization of a terrestrial magma ocean. *Journal of Geophysical Research*, *98*(E3), 5391–5406. https://doi.org/10.1029/92JE02579

Solomatov, V. S., & Stevenson, D. J. (1993b). Suspension in convective layers and style of differentiation of a terrestrial magma ocean. *Journal of Geophysical Research*, *98*(E3), 5375–5390. https://doi.org/10.1029/92JE02948

Sossi, P. A., Burnham, A. D., Badro, J., Lanzirotti, A., Newville, M., & O'Neill, H. S. (2020). Redox state of Earth's magma ocean and its Venus-like early atmosphere. *Science Advances*, *6*(48), eabd1387. https://doi.org/10.1126/sciadv.abd1387

Sossi, P. A., Tollan, P. M., Badro, J., & Bower, D. J. (2023). Solubility of water in peridotite liquids and the prevalence of steam atmospheres on rocky planets. *Earth and Planetary Science Letters*, *601*, 117894. https://doi.org/10.1016/j.epsl.2022.117894

Spaargaren, R. J., Ballmer, M. D., Bower, D. J., Dorn, C., & Tackley, P. J. (2020). The influence of bulk composition on the long-term interior-atmosphere evolution of terrestrial exoplanets. *Astronomy & Astrophysics*, *643*, A44. https://doi.org/10.1051/0004-6361/202037632

Spada, F., Demarque, P., Kim, Y. C., & Sills, A. (2013). The radius discrepancy in low-mass stars: Single versus binaries. *The Astrophysical Journal*, *776*(2), 87. https://doi.org/10.1088/0004-637X/776/2/87

Suer, T.-A., Jackson, C., Grewal, D. S., Dalou, C., & Lichtenberg, T. (2023). The distribution of volatile elements during rocky planet formation. *Frontiers in Earth Science*, *11*, 1159412. https://doi.org/10.3389/feart.2023.1159412

Tonks, W. B., & Melosh, H. J. (1993). Magma ocean formation due to giant impacts. *Journal of Geophysical Research*, *98*(E3), 5319–5333. https://doi.org/10.1029/92JE02726

Tsai, S.-M., Malik, M., Kitzmann, D., Lyons, J. R., Fateev, A., Lee, E., & Heng, K. (2021). A comparative study of atmospheric chemistry with Vulcan. *The Astrophysical Journal*, *923*(2), 264. https://doi.org/10.3847/1538-4357/ac29bc

Turbet, M., Bolmont, E., Chaverot, G., Ehrenreich, D., Leconte, J., & Marcq, E. (2021). Day-night cloud asymmetry prevents early oceans on Venus but not on Earth. *Nature*, *598*(7880), 276–280. https://doi.org/10.1038/s41586-021-03873-w

Turbet, M., Ehrenreich, D., Lovis, C., Bolmont, E., & Fauchez, T. (2019). The runaway greenhouse radius inflation effect. An observational diagnostic to probe water on Earth-sized planets and test the habitable zone concept. *Astronomy & Astrophysics*, *628*, A12. https://doi.org/10.1051/0004-6361/201935585

Turcotte, D. L., & Schubert, G. (2002). Geodynamics (2nd ed.). https://doi.org/10.2277/0521661862

Vazan, A., Ormel, C. W., Noack, L., & Dominik, C. (2018). Contribution of the core to the thermal evolution of sub-Neptunes. *The Astrophysical Journal*, *869*(2), 163. https://doi.org/10.3847/1538-4357/aaef33

Venturini, J., Guilera, O. M., Haldemann, J., Ronco, M. P., & Mordasini, C. (2020). The nature of the radius valley. Hints from formation and evolution models. *Astronomy & Astrophysics*, *643*, L1. https://doi.org/10.1051/0004-6361/202039141

Virtanen, P., Gommers, R., Oliphant, T. E., Haberland, M., Reddy, T., Cournapeau, D., et al., SciPy 1.0 Contributors. (2020). SciPy 1.0: Fundamental algorithms for scientific computing in Python. *Nature Methods*, *17*(3), 261–272. https://doi.org/10.1038/s41592-019-0686-2

Wadhwa, M. (2001). Redox state of Mars' upper mantle and crust from Eu anomalies in Shergottite pyroxenes. *Science*, *291*(5508), 1527–1530. https://doi.org/10.1126/science.1057594

Walters, D., Baran, A. J., Boutle, I., Brooks, M., Earnshaw, P., Edwards, J., et al. (2019). The Met Office Unified Model global atmosphere 7.0/7.1 and JULES global land 7.0 configurations. *Geoscientific Model Development*, *12*(5), 1909–1963. https://doi.org/10.5194/gmd-12-1909-2019

Wang, H. S., Lineweaver, C. H., & Ireland, T. R. (2018). The elemental abundances (with uncertainties) of the most earth-like planet. *Icarus*, *299*, 460–474. https://doi.org/10.1016/j.icarus.2017.08.024

Warren, P. H. (1985). The magma ocean concept and lunar evolution. *Annual Review of Earth and Planetary Sciences*, *13*(1), 201–240. https://doi.org/10.1146/annurev.ea.13.050185.001221

Warren, P. H., & Wasson, J. T. (1979). The origin of KREEP. *Reviews of Geophysics*, *17*(1), 73–88. https://doi.org/10.1029/RG017i001p00073

Western, C. M. (2017). Pgopher: A program for simulating rotational, vibrational and electronic spectra. *Journal of Quantitative Spectroscopy and Radiative Transfer*, *186*, 221–242. (Satellite Remote Sensing and Spectroscopy: Joint ACE-Odin Meeting, October 2015). https://doi.org/10.1016/j.jqsrt.2016.04.010

Western, C. M., Carter-Blatchford, L., Crozet, P., Ross, A. J., Morville, J., & Tokaryk, D. W. (2018). The spectrum of N2 from 4,500 to 15,700 cm^{-1} revisited with PGOPHER. *Journal of Quantitative Spectroscopy and Radiative Transfer*, *219*, 127–141. https://doi.org/10.1016/j.jqsrt.2018.07.017

Williams, C. D., & Mukhopadhyay, S. (2019). Capture of nebular gases during Earth's accretion is preserved in deep-mantle neon. *Nature*, *565*(7737), 78–81. https://doi.org/10.1038/s41586-018-0771-1

Wolf, A. S., Jäggi, N., Sossi, P. A., & Bower, D. J. (2023). VapoRock: Thermodynamics of vaporized silicate melts for modeling volcanic outgassing and magma ocean atmospheres. *The Astrophysical Journal*, *947*(2), 64. https://doi.org/10.3847/1538-4357/acbcc7

Wordsworth, R., & Kreidberg, L. (2022). Atmospheres of rocky exoplanets. *Annual Review of Astronomy and Astrophysics*, *60*(1), 159–201. https://doi.org/10.1146/annurev-astro-052920-125632

Wordsworth, R. D., Schaefer, L. K., & Fischer, R. A. (2018). Redox evolution via gravitational differentiation on low-mass planets: Implications for abiotic oxygen, water loss, and habitability. *The Astronomical Journal*, *155*(5), 195. https://doi.org/10.3847/1538-3881/aab608

Xu, S., & Bonsor, A. (2021). Exogeology from polluted white dwarfs. *Elements*, *17*(4), 241–244. https://doi.org/10.2138/gselements.17.4.241

Yurchenko, S. N., Amundsen, D. S., Tennyson, J., & Waldmann, I. P. (2017). A hybrid line list for CH4 and hot methane continuum. *Astronomy & Astrophysics*, *605*, A95. https://doi.org/10.1051/0004-6361/201731026

Yurchenko, S. N., Mellor, T. M., Freedman, R. S., & Tennyson, J. (2020). ExoMol line lists – XXXIX. Ro-vibrational molecular line list for CO_2. *Monthly Notices of the Royal Astronomical Society*, *496*(4), 5282–5291. https://doi.org/10.1093/mnras/staa1874

Yurchenko, S. N., & Tennyson, J. (2014). ExoMol line lists – IV. The rotation–vibration spectrum of methane up to 1500 K. *Monthly Notices of the Royal Astronomical Society*, *440*(2), 1649–1661. https://doi.org/10.1093/mnras/stu326

Zahnle, K. J., Lupu, R., Catling, D. C., & Wogan, N. (2020). Creation and evolution of impact-generated reduced atmospheres of early earth. *The Planetary Science Journal*, *1*(1), 11. https://doi.org/10.3847/PSJ/ab7e2c

Zhang, M., Knutson, H. A., Wang, L., Dai, F., dos Santos, L. A., Fossati, L., et al. (2022). Detection of ongoing mass loss from HD 63433c, a young mini-neptune. *The Astronomical Journal*, *163*(2), 68. https://doi.org/10.3847/1538-3881/ac3f3b

Zieba, S., Kreidberg, L., Ducrot, E., Gillon, M., Morley, C., Schaefer, L., et al. (2023). No thick carbon dioxide atmosphere on the rocky exoplanet TRAPPIST-1 c. *Nature*, *620*(7975), 746–749. https://doi.org/10.1038/s41586-023-06232-z

Zilinskas, M., Miguel, Y., van Buchem, C. P. A., & Snellen, I. A. G. (2023). Observability of silicates in volatile atmospheres of super-earths and sub-Neptunes - Exploring the edge of the evaporation desert. *Astronomy & Astrophysics*, *671*, A138. https://doi.org/10.1051/0004-6361/202245521